

2024-05-01

## Effect of the Microstructure on the Corrosion Behavior of AlCuNiMn and AlCuNiMnSi high entropy alloys in a 3.5wt% NaCl solution

Celine Chiong  
*University of Texas at El Paso*

Follow this and additional works at: [https://scholarworks.utep.edu/open\\_etd](https://scholarworks.utep.edu/open_etd)



Part of the [Mechanics of Materials Commons](#)

---

### Recommended Citation

Chiong, Celine, "Effect of the Microstructure on the Corrosion Behavior of AlCuNiMn and AlCuNiMnSi high entropy alloys in a 3.5wt% NaCl solution" (2024). *Open Access Theses & Dissertations*. 4077.  
[https://scholarworks.utep.edu/open\\_etd/4077](https://scholarworks.utep.edu/open_etd/4077)

This is brought to you for free and open access by ScholarWorks@UTEP. It has been accepted for inclusion in Open Access Theses & Dissertations by an authorized administrator of ScholarWorks@UTEP. For more information, please contact [lweber@utep.edu](mailto:lweber@utep.edu).

EFFECT OF THE MICROSTRUCTURE ON THE CORROSION BEHAVIOR OF  
ALCUNIMN AND ALCUNIMNSI HIGH ENTROPY ALLOYS  
IN A 3.5WT% NAACL SOLUTION

CELINE CHIONG

Master's Program in Metallurgical and Materials Engineering

APPROVED:

---

Stella A. Quinones, Ph.D., Chair

---

S.K. Varma, Ph.D.

---

Carlos Cabrera, Ph.D.

---

Suresh Divi, Ph.D.

---

Stephen L. Crites, Jr., Ph.D.  
Dean of the Graduate School

Copyright 2024 Celine Chiong

## **Dedication**

I dedicate this thesis to my family. As I am eternally grateful to my parents, as without their endless love, encouragement, and support, I wouldn't be where I am today. Throughout their time raising me, they have always pushed me to conquer my dreams and never let me give up when faced with new battles. Not once did their belief in me falter, in no doubt in their minds – they always believe I can do it. Especially through rough and challenging times, thank you for always having my back and believing in me.

EFFECT OF THE MICROSTRUCTURE ON THE CORROSION BEHAVIOR OF  
ALCUNIMN AND ALCUNIMNSI HIGH-ENTROPY ALLOY  
IN A 3.5WT% NACL SOLUTION

by

CELINE CHIONG, B.S.

THESIS

Presented to the Faculty of the Graduate School of

The University of Texas at El Paso

in Partial Fulfillment

of the Requirements

for the Degree of

MASTER OF SCIENCE

Department of Metallurgical, Materials, Biomedical Engineering

THE UNIVERSITY OF TEXAS AT EL PASO

May 2024

## **Acknowledgements**

Words cannot express how thankful I am to my committee for their continued support and encouragement: Dr. Stella Quinones, my committee chair, Dr. S.K. Varma, Dr. Suresh Divi, and Dr. Carlos Cabera. Dr. Quinones, your faith in my abilities has driven me to achieve more than I thought I possibly could. I cannot thank you enough for your generosity, effort, and resources you have invested in me and my research. Thank you for taking me as your advisee. I wanted to take the time to thank Dr. Christopher Bradley for your excellent lectures and teaching throughout the years. Starting with the course I have taken with you, Introduction to Metallurgical and Materials Engineering to Metallography and Microstructural Interpretation. Your comprehensive knowledge and honest feedback have provided me with insights and played an essential role in my academic journey. In addition, I would like to show my appreciation to Freeport-McMoRan for their financial support (Freeport-McMoRan Distinguished Chair Endowment in Metallurgical Engineering) and Stress Engineering Services for providing essential training in corrosion engineering design, analysis, and testing provided by Dr. Suresh Divi that made this research possible.

## Abstract

In this study, the AlCuNiMn and AlCuNiMnSi high entropy alloys (HEAs) are investigated to characterize the effect of Si addition and subsequent annealing treatments on the corrosion behavior in a 3.5wt% NaCl solution at room temperature. The microstructure evolution from the as-received condition and after annealing at 600°C, 800°C, and 1000°C for 24 hours in air is examined. The microstructural transformation of HEAs is extensively reported in the literature. However, its impact on the corrosion resistance of HEAs has not received the same attention. In this study, an increase in the annealing temperature of the base AlCuNiMn alloy improved the corrosion resistance due to element redistribution and homogenization of the microstructure. Annealing resulted in the appearance of new microconstituents with a higher resistance to corrosion compared to the alloy in the as-received condition. Introducing Si to the AlCuNiMn alloy system enhances the corrosion resistance. The addition of Si alters the morphology of the microstructure in three noticeable ways: 1) a redistribution of the other four elements, 2) the appearance of a new MnSi-rich microconstituent, and 3) a decrease in the size of voids. The results indicate that the AlCuNiMnSi alloy in the as-received condition is the superior alloy compared to the base AlCuNiMn alloy as it possesses the best corrosion resistance to the 3.5wt% NaCl solution. The presence of the Ni-rich microconstituent with small traces of Si slows the dissolution rate of the alloy. However, the phase fraction of Ni begins to dwindle then dissipates when the annealing temperature is increased to 800°C, leading to a slight increase in the corrosion rate.

## Table of Contents

Dedication .....	iii
Acknowledgements .....	v
Abstract .....	vi
Table of Contents .....	vii
List of Tables .....	ix
List of Figures .....	xi
1. Introduction .....	1
2. Background .....	2
2.1 Corrosion .....	2
2.2 Alloying Effects on the Corrosion Behavior of CoCrFeNi-based HEAs .....	4
2.2.1 Aluminum .....	5
2.2.2 Copper .....	7
2.2.3 Tin .....	8
2.2.4 Manganese .....	10
2.2.5 Other elements .....	11
2.3 Other High-Entropy Alloy systems .....	12
2.4 Heat Treatment Effect on Corrosion Mechanism of HEAs .....	13
2.5 Non-BCC Al-Cu-Ni-Mn-Ni High-Entropy alloys .....	14
3. Experimental Details .....	16
3.1 Materials Preparation: Initial Surface Preparation and Annealing .....	17
3.2 Microstructure, Chemical, and Structural Characterization .....	19
3.3 Electrochemical Corrosion Experimentation .....	20
4. Results .....	21
4.1 Microstructures of As-received Alloys .....	21
4.1.1 Microstructures of As-received AlCuNiMn Alloy .....	21
4.1.2 Microstructures of As-received AlCuNiMnSi Alloy .....	23
4.1.3 Comparison of As-received AlCuNiMn and AlCuNiMnSi Alloys .....	24
4.2 Oxidation Formation and Microstructural Evolution from Heat Treatment Process .....	26

4.2.1	Oxide Formation in AlCuNiMn and AlCuNiMnSi .....	26
4.2.2	Microstructural Evolution of AlCuNiMn .....	28
4.2.3	Microstructure Evolution of AlCuNiMnSi .....	34
4.3	Corrosion Behavior .....	42
4.3.1	Corrosion Analysis of AlCuNiMn.....	43
4.3.1.1	Potentiodynamic Polarization Results .....	43
4.3.1.2	Microstructural Analysis of AlCuNiMn After Corrosion.....	45
4.3.2	Corrosion Analysis of AlCuNiMnSi.....	51
4.3.2.1	Potentiodynamic Polarization Results for AlCuNiMnSi .....	51
4.3.2.2	Microstructural Analysis of AlCuNiMnSi After Corrosion .....	53
4.3.3	Comparison .....	58
5.	Discussion .....	60
5.1	Impact of the Microstructure Evolution on the Corrosion Resistance of AlCuNiMn .....	60
5.2	Impact of the Microstructure Evolution on the Corrosion Resistance of AlCuNiMnSi .....	61
6.	Conclusions.....	63
	References.....	64
	Vita	68

## List of Tables

Table 1. Summary of the oxides formed in the AlCuNiMnSi HEA at 600, 700, and 800°C [50].	15
Table 2. Properties of constituent elements in the AlCuNiMn and AlCuNiMnSi alloys. ....	18
Table 3. Chemical compositions of the principal elements of the AlCuNiMn and AlCuNiMnSi alloy.....	19
Table 4. Summary of the constituent phase compositions in AlCuNiMn and AlCuNiMnSi. ....	26
Table 5. Summary of the oxides identified with XRD for each alloy in its respective annealing temperature. ....	28
Table 6. The phase composition of AlCuNiMn alloy at various annealing temperatures as identified by EDS.....	29
Table 7. The phase composition of AlCuNiMnSi alloy at various annealing temperatures as identified by EDS.....	34
Table 8. Average Point ID from EDS analysis Table corresponds with Figure 22. ....	39
Table 9. Summary of the elemental phase change in the identified binary and ternary phases of the AlCuNiMn and AlCuNiMnSi alloys.....	40
Table 10. Chemical composition of the CuNiMnSi-rich region with increasing annealing temperature. ....	41
Table 11. Summary of corrosion data for as received and annealed (600°C, 800°C, and 1000°C) AlCuNiMn Alloy in 3.5wt% NaCl solution.....	44
Table 12. Summary of XRD data for corrosion products on each AlCuNiMn sample based on annealing temperature. ....	51
Table 13. Summary of corrosion data for as received and annealed (600°C, 800°C, and 1000°C) AlCuNiMnSi Alloy in 3.5wt% NaCl solution.....	52

Table 14. Electrochemical corrosion properties of the as cast and annealed CoCrFeNiMo in  
3.5wt%NaCl solution at room temperature [35, 54]..... 63

## List of Figures

Figure 1. A typical potentiodynamic-polarization curve in a 3.5 weight percent (wt%) NaCl solution for the explanation of the parameters[8]. .....	4
Figure 2. SEM Backscattered electron (BSE) images of CoCrFeNiAl <sub>x</sub> (x = 0.3, 0.5, and 0.7) alloys: (a) Al <sub>0.3</sub> CoCrFeNi, (b) Al <sub>0.5</sub> CoCrFeNi, and (c) Al <sub>0.7</sub> CoCrFeNi [15].....	6
Figure 3. Potentiodynamic polarization curves of (a) CoCrFeNiAl <sub>x</sub> (x = 0, 0.25, 0.5, 1.0) in 0.5 M H <sub>2</sub> SO <sub>4</sub> solution and (b) CoCrFeNiAl <sub>x</sub> (x = 0.3, 0.5, 0.7) in 3.5 wt.% NaCl solution [14, 15, 5]. ..	7
Figure 4. SEM-BSE images of an as-received CoCrFeNiCu <sub>x</sub> : (a) x= 0.5 and (b) x= 1 [13]......	8
Figure 5. Linear Polarization curves of equiatomic CoCrFeNi alloy with and without additions of Al, Cu, and Sn along with the stainless-steel samples immersed in 0.6 M NaCl solution at room temperature [9]......	10
Figure 6. Processing flow chart of the experimental procedure for AlCuNiMn and AlCuNiMnSi alloys. ....	17
Figure 7. The as-received AlCuNiMn and AlCuNiMnSi samples from Plasmaterials, Inc. ....	18
Figure 8. Microstructures of the as-received AlCuNiMn with (a) SEM image in BSE mode, and (b) EDS scans for each element. ....	22
Figure 9. XRD pattern of the as received AlCuNiMn alloy. ....	22
Figure 10. Microstructure of the as-received condition of the AlCuNiMnSi with (a) SEM image in BSE mode and (b) EDS scans for each individual element.....	24
Figure 11. XRD pattern of the as-received AlCuNiMn alloy. ....	24
Figure 12. SEM images of the microstructures of the as received AlCuNiMn alloy in (a) BSE mode and (b) SE mode; and the AlCuNiMnSi in (c) BSE mode and (d) SE mode.....	25

Figure 13. XRD results showing oxide formations of the AlCuNiMn alloy at (a) 600°C, (b) 800°C, and (c) 1000°C, and the AlCuNiMnSi alloy at (d) 600°C, (e) 800°C, and (f) 1000°C. ....	28
Figure 14. Microstructure of the AlCuNiMn sample annealed at 600°C with (a) SEM image in BSE mode and (b) EDS scans for each individual element.....	30
Figure 15. Microstructure of the AlCuNiMn sample annealed at 800°C with (a) SEM image in BSE mode and (b) EDS scans for each individual element.....	31
Figure 16. Microstructure of the AlCuNiMn sample annealed at 1000°C with (a) SEM image in BSE mode and (b) EDS scans for each individual element.....	32
Figure 17. SEM images of the AlCuNiMn alloy in the (a) as received condition and (b-c) annealed at 600°C in BSE and SE mode, (d) 800°C, and (e-f) 1000°C in BSE and SE mode.....	33
Figure 18. Microstructure of the AlCuNiMnSi sample annealed at 600°C with (a) SEM image in BSE mode and (b) EDS scans for each individual element.....	35
Figure 19. Microstructure of the AlCuNiMnSi sample annealed at 800°C with (a) SEM image in BSE mode and (b) EDS scans for each individual element.....	36
Figure 20. AlCuNiMnSi alloy after heat treatment at 1000°C for trials #1 and #2 showing inner contents escaping from oxidized cube exterior.....	37
Figure 21. Microstructure of the AlCuNiMnSi sample annealed at 1000°C.....	38
Figure 22. Microstructure of the AlCuNiMnSi sample annealed at 1000°C with (a) SEM image in BSE mode and (b) EDS scans for each individual element.....	39
Figure 23. SEM images of the AlCuNiMnSi alloy in the (a) as cast condition and annealed (b) 600°C, (c) 800°C, and (d) 1000°C conditions. ....	42
Figure 24. Potentiodynamic polarization curves of the as received and annealed (600°C, 800°C, and 1000°C) AlCuNiMn Alloy in 3.5wt% NaCl solution. ....	44

Figure 26. Microstructure of the AlCuNiMn annealed at 600°C Al-Cu-Ni-Mn after immersion in 3.5 wt.% NaCl solution along with EDS analysis with individual element mapping. ....	47
Figure 27. XRD pattern of the AlCuNiMn (annealed at 600°C) after immersion in 3.5 wt.% NaCl solution.....	47
Figure 28. Microstructure of the AlCuNiMn (annealed at 800°C) after immersion in 3.5 wt.% NaCl solution along with EDS analysis with individual element mapping.....	48
Figure 29. XRD pattern of the AlCuNiMn (annealed at 800°C) after immersion in 3.5 wt.% NaCl solution.....	49
Figure 30. Microstructure of the AlCuNiMn (annealed at 1000°C prior to corrosion testing) after immersion in 3.5 wt.% NaCl solution along with EDS analysis with individual element mapping. ....	50
Figure 31. XRD pattern of the AlCuNiMn annealed at 1000°C Al-Cu-Ni-Mn after immersion in 3.5 wt.% NaCl solution.....	50
Figure 32. Potentiodynamic polarization curves of the as-received and annealed (600°C, 800°C, and 1000°C) AlCuNiMnSi Alloy in 3.5wt% NaCl solution. ....	52
Figure 33. SEM BSE micrograph of the as-received AlCuNiMnSi after immersion in 3.5 wt.% NaCl solution along with EDS analysis with individual element mapping.....	54
Figure 34. Microstructure of the corroded as-received AlCuNiMnSi with (a) BSE and (b) SE imaging with EDS scans of each individual element.....	54
Figure 35. XRD patterns of the AlCuNiMnSi for the as-received sample, the annealed sample at 600°C, and the annealed sample at 800°C after immersion in 3.5 wt.% NaCl solution.....	55
Figure 36. Microstructure of the AlCuNiMnSi annealed at 600°C after immersion in 3.5 wt.% NaCl solution along with EDS analysis with individual element mapping.....	56

Figure 37. Corroded surface of the annealed (at 600° C) AlCuNiMnSi with (a) BSE and (b) SE imaging at 200x, and with (c) BSE and (d) SE imaging at 400x.....	56
Figure 38. Microstructure of the AlCuNiMnSi annealed at 800°C after immersion in 3.5 wt.% NaCl solution along with EDS analysis with individual element mapping.....	57
Figure 39. Corroded microstructures of the a) as received, b) annealed at 600°C, and c) annealed at 800°C Al-Cu-Ni-Mn-Si HEA from chloride-ion attack. ....	58
Figure 40. Comparison of potentiodynamic curves for both the AlCuNiMn and AlCuNiMnSi alloys in the as received condition immersed in 3.5wt% NaCl solution at room temperature. ....	59
Figure 41. Corrosion rates of the AlCuNiMn and the AlCuNiMnSi alloys for samples in the as-received condition, and for samples annealed at various temperatures prior to corrosion testing. ....	59
Figure 42. Corrosion rate of AlCuNiMn as a function of annealing temperature with illustrations of sample surfaces before and after corrosion testing.....	61
Figure 43. Corrosion rate of AlCuNiMnSi as a function of annealing temperature with illustrations of sample surfaces before and after corrosion testing.....	62

## 1. Introduction

High-entropy alloys (HEAs) originated from a new metallurgical alloying strategy developed by Yeh et al. in 2004 [1] that resulted in excellent performance. The conventional manufacturing method for HEAs is arc-melting of five or more principal metallic elements in equiatomic or near-equiatomic proportions that results in a high entropy of mixing [2]. The HEAs differ from conventional alloys where the matrix consists of only one element. According to Yeh, the increase in entropy of mixing decreases the free energy, leading to the formation of simple solid solutions with the absence of complex phases. HEAs are known to exhibit four core effects: (1) high entropy (thermodynamics), (2) severe lattice distortion (structure), (3) a sluggish diffusion (kinetics), and (4) a cocktail effect (material properties) [2, 3, 4]. The focus on HEAs is due to the tailoring of desirable properties, such as high strength and ductility, high fracture toughness over a range of temperatures, high hardness, good structural stability, exceptional wear resistance, excellent high-temperature oxidation, and enhanced corrosion resistance [4, 5].

Although there are several definitions of HEAs, the general rule is that HEAs are made using 5 elements that result in common crystal structures (typically body-centered cubic (BCC), face-centered cubic (FCC), or hexagonal closed-packed (HCP)) [6]. The corrosion behavior of HEAs is unique due to the localized microstructural effects of high entropy alloying [7].

## 2. Background

### 2.1 CORROSION

The economic impact and the potential risk to public safety makes the study of corrosion of metals and alloys and the development of new corrosion-resistant materials a national priority. Corrosion of metallic materials is an irreversible electrochemical interaction between an alloy and its environment [8]. It can result in severe deterioration, and in some cases, rapid and catastrophic failure. Unexpected failures can place human lives at risk and have the potential to contaminate the environment. The economic cost of corrosion in the United States is estimated to be 6.2% of the U.S. gross domestic product and increased from \$276 billion in 1998 to \$1 trillion in 2013, (GDP) [8, 7]. The global cost of corrosion in 2013 was \$2.5 trillion, or 3.4% of the global GDP.

Corrosion resistance is the alloys' ability to resist damage and depends on the chemical reactions occurring on the surface and on the stability of the passive layer. The comparison of corrosion resistance across different HEA alloy systems needs to be examined further to make sure that the conditions for each study are reproducible and the characterization of the surface films are explored to accurately interpret the corrosion behavior [9]. At this time, only approximately 30 conventional alloy systems have been explored, whereas  $10^{11}$  HEAs have been investigated using 60 feasible elements. The total possible number of HEAs is  $10^{100}$ , making the design of high-entropy alloys (HEAs) [3], HEA composition, and examination processes of importance to the material community.

The definition of HEAs today are alloys with five or more major principal elements, each element having an atomic percentage in near equal proportions [3]. There are a variety of HEA systems that have been fabricated that exhibit higher corrosion resistance compared to conventional corrosion-resistant alloys. Conventional alloys include stainless steels, copper-nickel

alloys, nickel-based alloys, etc. Stainless steel is known for its corrosion resistance due to its high chromium (Cr) content (approximately 12-18%) and protective passive layer [10]. The corrosion behavior of conventional alloys is influenced by the microstructure and the formations of precipitates (e.g. carbides, nitrides, or intermetallics). Thermal joining processes of stainless steels, like welding, can result in the formation of  $M_{23}C_6$  carbides at the grain boundaries, which depletes the Cr content in other areas, making the depleted areas the anode of a microelectrochemical cell susceptible to localized corrosion [11]. Fortunately, these carbides can be diminished with heat treatments. HEAs tend to form solid solutions of common structures as a result of the high mixing entropy, typically body-centered cubic (BCC), face-centered cubic (FCC), and hexagonal closed-packed (HCP). The multiple-element HEA systems can result in several solid solutions with locally disordered structures that lead to unique corrosion-resistant properties [12].

The corrosion behavior of a material can be examined using a standard electrochemical method called potentiodynamic-polarization test. The polarization curve from this test can identify the corrosion potential ( $E_{corr}$ ), corrosion-current density ( $i_{corr}$ ), passive current density ( $i_{pass}$ ), and pitting potential ( $E_{pit}$ ) as illustrated in Figure 1 [8]. The  $E_{corr}$  value is a measure of the electronegativity of the material,  $i_{corr}$  is used to determine the corrosion rate using Faraday's Law,  $i_{pass}$  is the point where the current density levels off due to the formation of a protective passive film, and  $E_{pit}$  identifies the potential value where pits form on the surface.

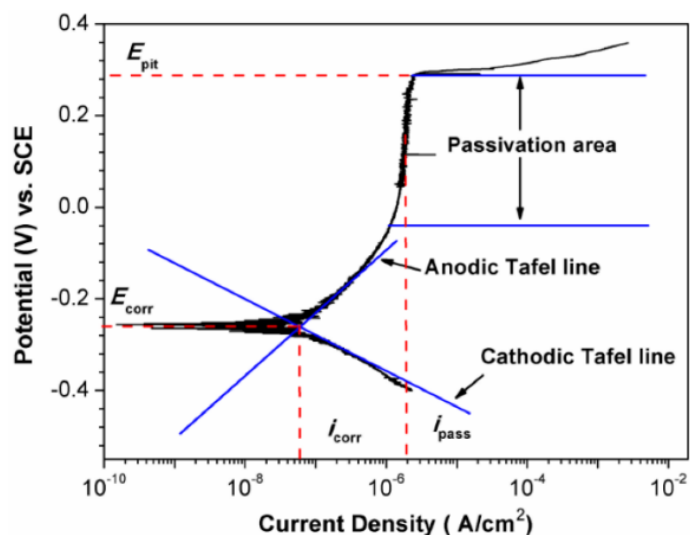


Figure 1. A typical potentiodynamic-polarization curve in a 3.5 weight percent (wt%) NaCl solution for the explanation of the parameters[8].

The HEA with a base composition of CoCrFeNi-x ( $x$  = fifth alloying element) is extensively studied in various aqueous solutions due to its remarkable corrosion resistance. Numerous studies describe the influence of the alloying elements, the microstructural phases (or microconstituents) and heat processing on the corrosion rate, preferential attack and corrosion products. An overview of this alloy is provided below since it may provide beneficial information for future designs of corrosion resistant HEAs.

## 2.2 ALLOYING EFFECTS ON THE CORROSION BEHAVIOR OF COCRFENI-BASED HEAS

Alloying with different elements affects the corrosion resistance of the alloy as it changes the phase structure, causes elemental segregation, and alters the protectiveness of the passive film. Li et al. [3] have documented specific elements that may be used for alloying HEAs and/or the benefit of their addition: (1) Co, Cr, Fe, Ni, Cu, and Mo have been extensively explored in single-FCC phase HEAs, (2) Al, Si, and Sn are introduced in varied concentrations to alter microstructures and/or properties, and (3) Mn plays a role in phase stability.

The CoCrFeNi system is a well-documented alloy that results in a single-phase face-centered cubic (FCC) solid solution structure with no apparent fluctuation in composition. It has

attracted the most attention compared to other alloy system, and it has already been confirmed, that in NaCl solutions, the CoCrFeNi alloy has distinctly better pitting resistance compared to 304L stainless steels [13]. Type-304 is the most common stainless steel while 316 comes in second. Both offer an immensely superior corrosion resistance in chloride and acidic solutions. Type 304 is the most versatile and used alloy in the chemical industry, food processing plants, cryogenic vessels, etc. The corrosion resistance of CoCrFeNi alloys in various aqueous environments has been examined with the addition of a fifth element [13, 14, 15, 9, 16, 17, 18].

This section analyzes the influence of alloying elements on the CoCrFeNi-based alloy in order to gain an understanding of the role each element plays on the corrosion behavior. It should be noted that the addition of a fifth alloying element has the potential to alter the microstructure in two ways: (1) the creation of a two-phase microstructure, i.e. the evolution of a second phase, and/or (2) the emergence of an entirely new single-phase microstructure [9]. These following sections will specifically review the alloying addition of Al, Cu, Sn, Mn, and other elements to CoCrFeNi. Consequently, the HEAs that are discussed in detail are CoCrFeNiAl, CoCrFeNiCu, CoCrFeNiSn, CoCrFeNiMn, and other alloys (such as CoCrFeNiW and CoCrFeNiMo). These alloys consist of equimolar or near-equimolar elemental fractions. This review describes how each element affects the corrosion behavior of the alloy as a result of changes in the microstructure and protectiveness of the passive oxide layer. The electrochemical properties of these alloys are reported in either chloride or sulfuric acid solutions using the potentiodynamic polarization method.

### **2.2.1 Aluminum**

Adding elements (such as aluminum, chromium, cobalt and nickel) serve to form and enhance the performance of oxide passivation films that decrease the corrosion rate. Aluminum

(Al) additions have proven to boost the protection of the passive layer in Ni-based alloys [19]. As for HEAs, Al addition reduces the overall density of the alloy and improves the alloy's mechanical properties [20, 21, 22]. Kao et al. [14] studied the corrosion behavior of  $\text{CoCrFeNiAl}_x$  ( $x = 0, 0.25, 0.50, 1.0$ ) in 0.5 M sulfuric acid solution while Shi et al. [15] studied the influence of Al on the passive film of  $\text{CoCrFeNiAl}_x$  ( $x = 0.3, 0.5, 0.7$ ) in 3.5wt% NaCl solution. It was found that Al alloying has a significantly effect on the evolution of the phase microstructure. Increasing the Al content results in the formation of a BCC phase. The microstructure evolution is from a single FCC phase to a duplex phase (retained FCC + BCC), and eventually to a BCC + B2 (an ordered BCC phase) [5]. Figure 2 illustrates the phase evolution as the Al content is increased from  $x = 0.3$  to  $x = 0.7$ . The increase in Al content increases the formation of a Cr depleted (Al-Ni) rich phase with poor resistance to  $\text{Cl}^-$  ion attack and a higher probability of pit formation. The growth of a weak passive film also occurs with an increase in Al content.

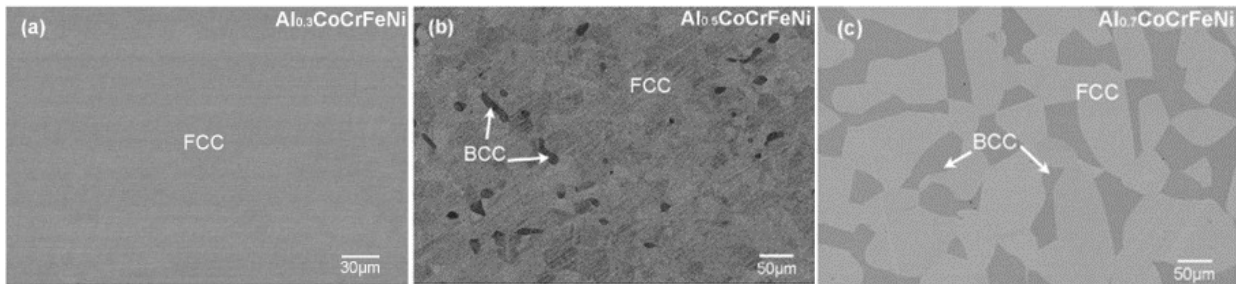


Figure 2. SEM Backscattered electron (BSE) images of  $\text{CoCrFeNiAl}_x$  ( $x = 0.3, 0.5, \text{ and } 0.7$ ) alloys: (a)  $\text{Al}_{0.3}\text{CoCrFeNi}$ , (b)  $\text{Al}_{0.5}\text{CoCrFeNi}$ , and (c)  $\text{Al}_{0.7}\text{CoCrFeNi}$  [15].

The potentiodynamic polarization curves of  $\text{CoCrFeNiAl}_x$  in different aqueous solutions are shown in Figure 3. Increasing the Al content decreases the overall corrosion resistance of  $\text{CoCrFeNiAl}_x$ . In a 0.5 M  $\text{H}_2\text{SO}_4$  solution, an increase in the Al content increases the passive current density and maintains the same corrosion potential and passive region. Exposure to the 3.5wt% NaCl solution results in more severe consequences, where the passive current density increases, the corrosion potential becomes more negative, and shrinking of the passive region

occurs. These factors indicate that increasing the Al concentration within this HEA system has negative consequences on the corrosion behavior, especially when exposed to chloride-containing solutions compared to sulfuric acid solutions [5].

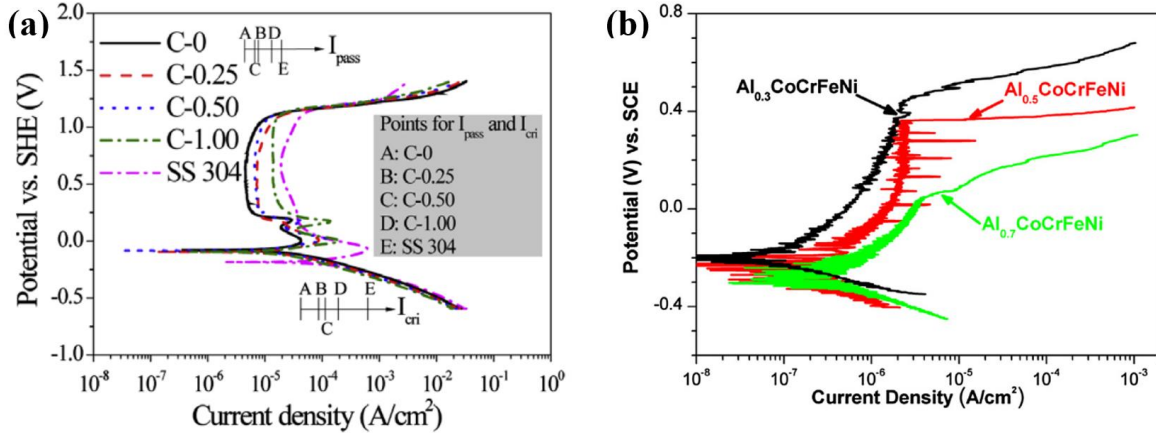


Figure 3. Potentiodynamic polarization curves of (a)  $\text{CoCrFeNiAl}_x$  ( $x = 0, 0.25, 0.5, 1.0$ ) in 0.5 M  $\text{H}_2\text{SO}_4$  solution and (b)  $\text{CoCrFeNiAl}_x$  ( $x = 0.3, 0.5, 0.7$ ) in 3.5 wt.% NaCl solution [14, 15, 5].

When this alloy is immersed in the 3.5 wt. % NaCl solution, the  $\text{Cl}^-$  ions in solution absorb on the passive film and combine with Al containing metastable ion complexes that dissolve in the solution. Increasing the Al content is reported to cause a decrease in the Cr content in the passive film and an increase in the proportion of Al oxide/Al hydroxide, leading to the formation of a porous film which is unable to offer a protective barrier to the chloride ion attack [5, 15].

### 2.2.2 Copper

The use of copper (Cu) as the base alloy and in moderate concentrations (such as in Cu-Ni alloys and 304 stainless steels) has shown both exceptional corrosion resistance and mechanical properties [23, 24]. Numerous researchers have investigated the effect Cu on the corrosion resistance of HEAs. Hsu et al. [13] studied the effect of Cu on the corrosion resistance of  $\text{CoCrFeNi}$  in a 3.5 wt% NaCl solution. It was reported that the addition of Cu resulted in a two-phase FCC

structure. The large positive enthalpy of mixing of Cu with other constituents results in Cu segregation in the major FCC phase [25]. An as-received CoCrFeNiCu<sub>x</sub> HEA with Cr-rich dendrites and Cu-rich inter-dendrites (Cr-depleted) is shown in Figure 4.

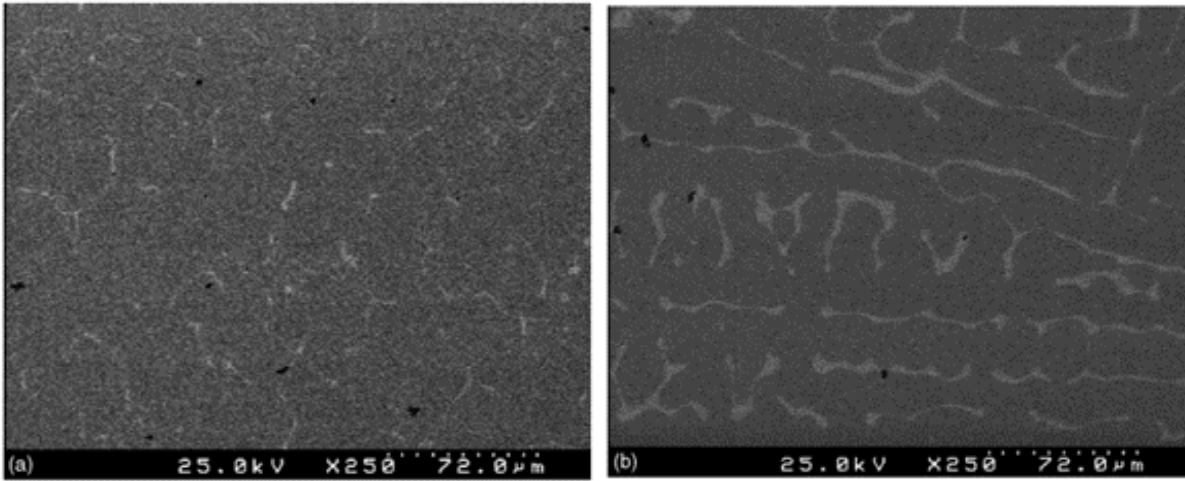


Figure 4. SEM-BSE images of an as-received CoCrFeNiCu<sub>x</sub>: (a) x= 0.5 and (b) x= 1 [13].

Ultimately, the microstructure develops a potential difference between the dendrites and the active Cr-depleted inter-dendrite regions resulting in galvanic corrosion between the two regions. An increase in the Cu concentration deteriorates the corrosion resistance and accelerates the damage to CoCrFeNiCu<sub>x</sub> alloys. Higher corrosion and pitting potentials for the CoCrFeNi and the 304 stainless steel alloy are due to the segregation of Cu. Thus, the addition of Cu produces a non-protective film, and the continued increase of Cu content narrows the passivation region and increases the passivation current.

### 2.2.3 Tin

Tin (Sn) is corrosion resistant and has low toxicity, a low melting point, ease of alloying, and is traditionally used for Cu hardening to form a much harder bronze alloy [26]. Because of its corrosion resistance, Sn is applied to coatings for corrosion protection. Microalloying of the FeCoNiCu alloy with small Sn concentrations improves the pitting corrosion resistance in chloride solutions [27]. Muangtong et al. [9] describes the corrosion behavior of equiatomic CoCrFeNi

alloys with additions of Al, Cu, and Sn and compares the results with two standard stainless steels in a 0.6 M NaCl solution. Like CoCrFeNiCu<sub>x</sub>, the Sn-containing HEA leads to the formation of a second phase structure. In the case of Sn, the FCC phase is retained, and a NiSn-rich hexagonal structure is introduced. This new phase formation evolves due to the mixing enthalpy of different atomic pairs. The NiSn couple has a strong bond and has the largest negative enthalpy of mixing value compared to the other elements (Al and Cu). Figure 5 is a comparison of potentiodynamic scans for CoCrFeNi alloys, 304 stainless steel, and 316 stainless steels. The addition of Al and Cu (to form equiatomic CoCrFeNiAl and CoCrFeNiCu), results in a decrease in the corrosion resistance, confirming the reports from the literature, but with a more severe result in this instance. In the case of Sn addition (to form equiatomic CoCrFeNiSn), the corrosion resistance is superior to the CoCrFeNi alloy. The alloy with Sn demonstrates the largest passive region and highest pitting potential compared to the other alloys. This indicates the presence of a strong oxide film formation. The three HEA systems form two passive films, a Cr<sub>2</sub>O<sub>3</sub> is present in all three, and the second film is either Al<sub>2</sub>O<sub>3</sub>, Cu<sub>2</sub>O, or SnO<sub>2</sub>. The Cr<sub>2</sub>O<sub>3</sub> film is known to be a very stable, strong, and corrosion-resistant oxide resistant to chloride attack. However, the addition of Al and Cu tends to reduce the formation of Cr<sub>2</sub>O<sub>3</sub>, and both Al<sub>2</sub>O<sub>3</sub> and Cu<sub>2</sub>O are unstable and break down more easily. The SnO<sub>2</sub> is the most stable film with a high potential for Cl<sup>-</sup> ion attack [9, 28]. The FCC phase (CuCrFeNi-rich) in CuCrFeNiSn corrodes due to the galvanic couple with the Ni-Sn phase. Overall, the corrosion resistance improves with the addition of Sn as illustrated in Figure 5.

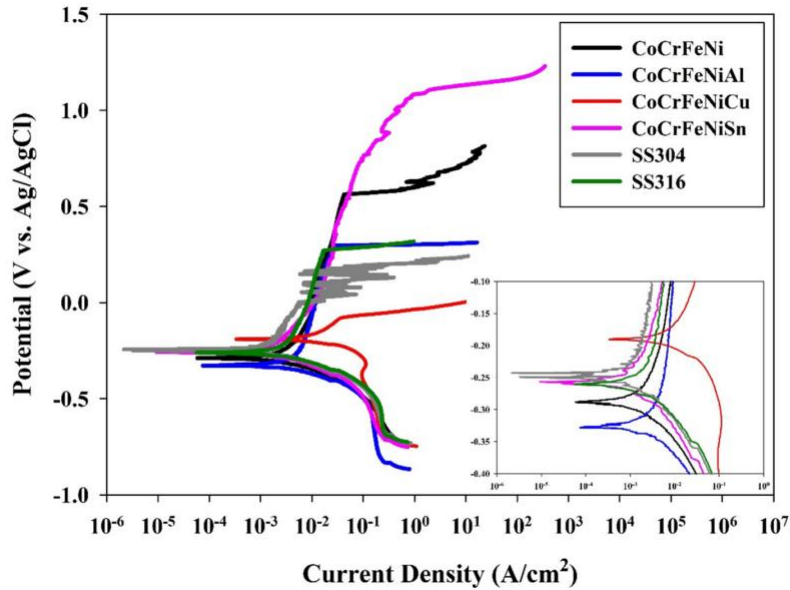


Figure 5. Linear Polarization curves of equiatomic CoCrFeNi alloy with and without additions of Al, Cu, and Sn along with the stainless-steel samples immersed in 0.6 M NaCl solution at room temperature [9].

#### 2.2.4 Manganese

In 2004, Cantor developed an equiatomic CoCrFeNiMn alloy with a single FCC solid solution [16]. The phase stability of this alloy (and thermal expansion, mechanical properties and oxidation resistance) resulting from the inclusion of Mn is well documented [29, 30, 31]. Zhang et al. [17] compared the microstructures of CoCrFeNiMn and CoCrFeNi alloys. The microstructure of both alloys includes equiaxed grains, but the CoCrFeNiMn alloy also contains spherical inclusions. Based on previous literature, the inclusions contain traces of MnO and MnS and are responsible for the onset of corrosion [32]. Mn also increases the grain size, which decreases the overall grain boundary area [17]. The influence of the microstructure on corrosion resistance is not fully understood, including the impact of grain size, grain boundary, and the distribution of the second phase [5]. The corrosion potential of CoCrFeNiMn is lower than that of CoCrFeNi, and its corrosion current density is much larger, and thus has a much higher tendency to corrode. Its passive film contains large amounts of Mn (with lower amounts of Co, Cr and Fe), and the Mn

reduces the stability of the passive film and accelerates the corrosion rate in chloride-containing solutions. In conclusion, the corrosion resistance of the equiatomic CoCrFeNiMn alloy is inferior to CoCrFeNi in both chloride and sulfuric acid solutions [17, 33, 34].

### 2.2.5 Other elements

Aluminum, copper, tin and manganese elements all have low melting temperatures and contain a non-BCC crystal structure. Additional alloying elements of the CoCrFeNi material include tungsten and molybdenum (W and Mo). These elements are chosen because they: (1) have a large difference in atomic radius compared to other constituents in this alloy system; (2) are refractory elements with extremely high melting points; and (3) have a BCC crystal structure.

Studies show that the addition of W and Mo increases the resistance to pitting corrosion. The additions of W to CoCrFeNiW<sub>x</sub> with (x = 0, 0.2, 0.5) transforms the single-FCC phase to a dual-FCC phase structure with (FeCoCr)<sub>7</sub>W<sub>6</sub> precipitates [18]. This phase separation is due to tungsten's large atomic size. The resulting microstructure also includes dendritic and interdendritic structures. The addition of W to CoCrFeNi improves the pitting resistance in addition to its passivation behavior in seawater solutions. The CoCrFeNiW<sub>0.5</sub> alloy performs best compared to the CoCrFeNiW<sub>0.2</sub> and CoCrFeNi, with wider passive regions and lower passivation current density values, along with improved mechanical properties. This level of W addition (x=0.5) is thought to produce the most stable passivation layer.

The alloying of CoCrFeNi with Mo also improves the corrosion resistance [22, 35, 36]. Wang et al [35] highlights the excellent pitting resistance and higher corrosion resistance of CoCrFeNiMo<sub>0.2</sub> in a 3.5wt% NaCl solution compared to 304 SS. Dai et al [36] studied the influence of Mo addition on the passive film by investigating the corrosion mechanism of CoCrFeNiMo<sub>x</sub> (x = 0, 0.1, 0.3, 0.6) alloys. Like the formation of the passive film on a 304 stainless

steel, the passive film exhibits a double-layer structure composed of an inner layer of Cr oxides/hydroxides and an outer layer of Cr/Fe oxides/hydroxides [5]. A small addition of Mo positively impacts the ratio of  $\text{Cr}_2\text{O}_3/\text{Cr}(\text{OH})_3$  and reduces the point defect density. The integration of Mo oxides in the film also improves the corrosion resistance of  $\text{CoCrFeNiMo}_x$  compared to the CoCrFeNi base alloy, especially in NaCl solutions [22].

### 2.3 OTHER HIGH-ENTROPY ALLOY SYSTEMS

The use of Al, Cu, and Mn elements in the CoCrFeNi base system (in small quantities or in equal amounts as the other constituents) all have one similar effect that leads to Cr depletion within the phases and passivating layer, making it prone to chloride ion attack. The oxide film of the Al and Cu additions reduced the Cr oxide formation and increase the development of an unstable and weak Al/Cu oxide. Sn is the only one of the four low melting temperature elements to improve the corrosion resistance due to the generation of  $\text{SnO}_2$  which is an already proclaimed passive layer that has been effectively used in preventing corrosion. In contrast to previous literature studying different HEA systems, Al addition did not negatively affect the corrosion properties of  $\text{CrFeMoVAI}_x$  ( $x = 0, 0.2, 0.6, 1$ ) [37] and  $\text{CoCuFeNiTiAl}_x$  ( $x = 0, 0.25, 0.5, 0.75, 1$ ) [38] in 3.5wt% NaCl solution. Even with minor additions of Al, the corrosion resistance of  $\text{CoCuFeNiTiAl}_{0.25}$  increased so much so that they can be candidates for severe marine and acidic environments. The use of Cu in HEAs tends to stabilize the FCC phase, but an excessive amount of Cu causes elemental segregation which leads to inter-dendritic regions and possible localized corrosion attack [39, 40]. Moreover, Zhou et al. [4, 41] prepared a  $\text{CoCrCuFeNiAl}_{0.4}$  HEA with high amounts of Cu. When submerged into an aqueous marine solution, the HEA releases a large quantity of Cu, thus hindering bacteria growth and increasing biofilm formation. Thus, it can be concluded that, different HEA systems, with different quantities of alloying element(s) will vary

their corrosion resistance properties. Within the literature in this section, it was noticed that Al and Cu additions improved the corrosion resistance but contained a higher ratio of refractory metals to elements in the system.

## **2.4 HEAT TREATMENT EFFECT ON CORROSION MECHANISM OF HEAS**

Heat treatment is a procedure of applying heat to a material and then cooling in a controlled manner for the purpose of enhancing the material's performance, durability, and properties. Heat treatments involve two major factors: (1) heating temperatures and (2) cooling rates. These parameters will influence the microstructure and properties of the material. The appropriate heat treatment can create a uniform microstructure and elemental distribution [5]. It is believed that a more uniform microstructure can enhance the corrosion resistance. Researchers have mostly focused on the as-received condition of HEAs, which are more inclined to contain defects or voids. Reports from the literature indicate that heat treatments (at higher temperatures) tend to homogenize the microstructures. Lin et al. [42] were able to successfully dissolve a Cu-rich phase into an FCC matrix by aging a  $\text{Cu}_{0.5}\text{CoCrFeNi}$  HEA at  $1250^\circ\text{C}$  for 24 hours. This dissolution reduces the Cu segregation within the microstructure which lowers the corrosion rate of the  $\text{Cu}_{0.5}\text{CoCrFeNi}$  HEA in 3.5wt% NaCl solution. Additionally, subjecting  $\text{AlFeNiCoCuCr}$  to remelting and annealing increases the pitting corrosion resistance [43]. Annealing this alloy from the as-received condition at  $1000^\circ\text{C}$  for 3 hours reduces the pit size, produces larger dendrite regions, and decreases the Cu segregation in the inter-dendritic regions, resulting in a decrease in the corrosion rate. Zhang et al. [43] reports that the annealing treatment more positively influences the corrosion resistance compared to a remelting treatment. Likewise, similar results from Masemola et al. [44] found that the equiatomic  $\text{AlCrFeMnNi}$  annealed between  $400\text{-}1000^\circ\text{C}$  for 2 hours displays considerable resistance to corrosion compared to the alloy in the as-received

condition. The as-received microstructure, with Cr-rich dendrite regions and Al-Ni-rich interdendritic regions (ordered BCC (B2) phase), transitions to an FCC phase with coarsening of grains and a decreased volume fraction of the BCC phase. However, high temperature annealing at 1000°C increases the corrosion rate due to the combination of the new FCC phase with the already existing BCC phase causes localized chemical inhomogeneity that leads to a galvanic effect. In summary, heat treatments can improve the corrosion resistance of HEAs by reducing elemental segregation and improving the uniformity of the microstructure. However, not all heat treatments yield the same corrosion resistant properties.

## **2.5 NON-BCC AL-CU-NI-MN-NI HIGH-ENTROPY ALLOYS**

A widely used definition of “refractory element” is an element that has a high melting temperature (greater than 1850°C) and generally has a BCC crystal structure [45]. Some examples of refractory metals include W, Nb, Re, Ta, V, Cr, and Mo. Refractory elements are usually used to create a BCC-structured refractory HEAs while HEAs with more commodity elements form either FCC structures, BCC structures, or a combination of both FCC and BCC structures [46]. HEAs with BCC structures have drawn considerable attention for high-temperature applications [47, 48, 49]. For instance, Varma et al. [48] studied the oxidation resistance of a NbCrVWTa HEA, Gorr et al. [49] investigated the high-temperature oxidation behavior of an equimolar NbMoCrTiAl HEA with and without Si addition, etc. Efforts to improve the high-temperature oxidation resistance of these promising candidates include the addition of Cr, Al, Si, and/or other elements. Hitter et al. [50] investigated the opposite of this approach and produced a non-BCC HEA intended for low-temperature applications. The study characterized the microstructure and oxidation behavior in air at 600, 700, and 800°C of an equiatomic quaternary AlCuNiMn alloy and AlCuNiMnSi HEA alloy. Hitter et al. describes the importance of creating advanced materials for

low and medium temperature ranges. The BCC alloys have the upper hand in obtaining higher melting temperatures, however, the FCC alloys are more easily fabricated and have higher ductility. HEAs with a single phase, especially an FCC structure, have better corrosion resistance compared to multi-phase HEAs. Hitter et al. reported that AlCuNiMn contains microstructures with at least three constituents (AlCuNi-rich, Ni-rich, and Mn-rich). The addition of Si redistributes the composition of the three regions and decreases the oxidation resistance compared to the AlCuNiMn alloy. Various annealing treatments (600, 700 and 800°C) formed oxides in the AlCuNiMnSi HEA (Table 1). Intermetallics in these alloys did not oxidize.

Table 1. Summary of the oxides formed in the AlCuNiMnSi HEA at 600, 700, and 800°C [50].

600°C	700°C	800°C
Mn <sub>2</sub> O <sub>3</sub> Cu(Cu <sub>0.55</sub> Mn <sub>1.5</sub> )O <sub>4</sub>	Mn <sub>2</sub> O <sub>3</sub> Cu <sub>1.4</sub> Mn <sub>1.6</sub> O <sub>4</sub> Cu <sub>4</sub> O <sub>3</sub>	Mn <sub>2</sub> O <sub>3</sub> CuMn <sub>2</sub> O <sub>4</sub> Cu <sub>4</sub> O <sub>3</sub>

Yang et al. [51] studied the effect of Si addition on the corrosion resistance of an Al<sub>0.2</sub>CoCrFe<sub>1.5</sub>Ni dual-phase (FCC + BCC) HEA in a saline solution. Trace element of Si help retain the single FCC phase which in turn improves the corrosion resistance. Higher Si content leads to the formation of a BCC phase structure in the inter-dendritic regions of Al<sub>0.2</sub>CoCrFe<sub>1.5</sub>NiSi<sub>x</sub> (for x = 0.2 and 0.3). With increasing Si content, the volume fraction of the BCC phase (AlNiSi-rich and Cr-depleted) increases, leading to galvanic corrosion and deteriorated corrosion resistance. A dual phase structure is also observed for the CrFeNiAl<sub>0.28</sub>Si<sub>0.12</sub> HEA [52] with larger proportions of the FCC phase (Fe-Ni-rich) compared to the BCC phase (Al-Cr-rich). Due to larger amounts of the FCC phase, this CrFeNiAl<sub>0.28</sub>Si<sub>0.12</sub> HEA exhibited high strength, good plasticity, and excellent corrosion resistance in a 3.5wt% NaCl solution, almost comparable to 304 stainless steel.

Overall, this review has explored multiple HEA systems to provide a guide on how the alloys' behavior changes with the addition of low temperature alloying elements, and that there is a lack of information on the corrosion behavior of non-BCC HEA systems that needs to be explored.

### **3. Experimental Details**

The goal of this work is to expand on the work by Hitter et al. by investigating the influence of annealing temperature on the microstructure and consequently, on the effect of the microstructure on the corrosion resistance. It is expected that the results from this study may influence future alloy design considerations.

Figure 6 includes a schematic of the experimental procedure for the study of AlCuNiMn and AlCuNiMnSi alloys. Samples are divided into two groups. The first group includes the as-received samples for each alloy, and after their microstructures are examined, they are reserved for the corrosion study. The second group of samples undergo annealing treatments at temperatures of 600, 800 and 1000°C, and the effect of these thermal treatments on the corrosion behavior is examined.

Samples in the first group (as-received) are characterized by scanning electron microscopy (SEM) and energy-dispersive spectroscopy (EDS) for chemical analysis. Samples in the second group are subjected to varying heat treatments that modify the microstructure. Microstructural changes due to annealing are identified using SEM and EDS characterization. Corrosion testing determines the influence of the annealing temperature on the corrosion rate during exposure to 3.5wt% NaCl solution at room temperature. Each of the procedures in Figure 1 are explained in detail in sections 3.1 through 3.3.

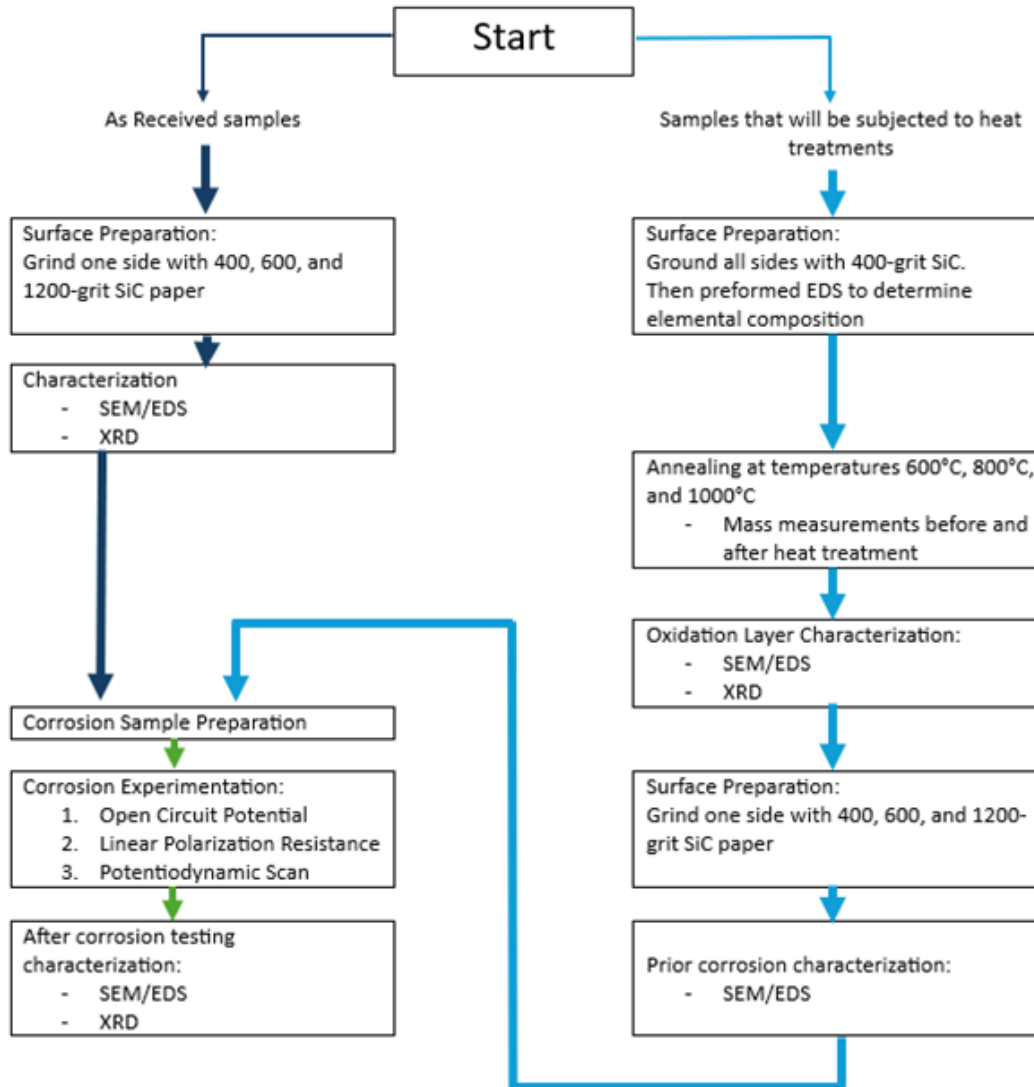


Figure 6. Processing flow chart of the experimental procedure for AlCuNiMn and AlCuNiMnSi alloys.

### 3.1 MATERIALS PREPARATION: INITIAL SURFACE PREPARATION AND ANNEALING

The AlCuNiMn and AlCuNiMnSi alloys are manufactured by Plasmaterials, Inc. (Livermore, California USA) using arc melting to guarantee complete melting and chemical homogeneity before being cast. Electrical discharge machining (EDM) is used to shape the cast material into cubes with 5 mm dimensions on each side. Table 2 includes a list of the structural and physical properties for each of the non-BCC metals used to manufacture these alloys.

Table 2. Properties of constituent elements in the AlCuNiMn and AlCuNiMnSi alloys.

Element	Aluminum	Copper	Nickel	Manganese	Silicon
Crystal Structure	FCC	FCC	FCC	Cubic	Diamond Cubic
Melting Point (°C)	660	1084	1455	1244	1410
Atomic Radius (Å)	1.432	1.278	1.243	1.12	1.176
Density (g/cm <sup>3</sup> )	2.70	8.92	8.908	7.47	2.33
Valence	+3	+2/+3	+2	+3/+4	+4

\*The valence value for Cu and Mn is assumed to be +3 and +4 for AlCuNiMn annealed at 1000°C based on the presence of Cu<sub>4</sub>O<sub>3</sub> and Mn<sub>3</sub>O<sub>3</sub>.

The surface of the samples in the as-received condition consists of a rough linear textured pattern as illustrated in Figure 7. The first step is to prepare the surface of each face of the metal cube for annealing by smoothing the surface with a 400-grit SiC paper to remove the rough textured surface. The chemical composition for all specimens is examined using EDS to identify the level of consistency of each element. Table 3 lists the near-equiatomic proportions of both alloys, in atomic percent, and is compared to the reported values from Plasmaterials, Inc.

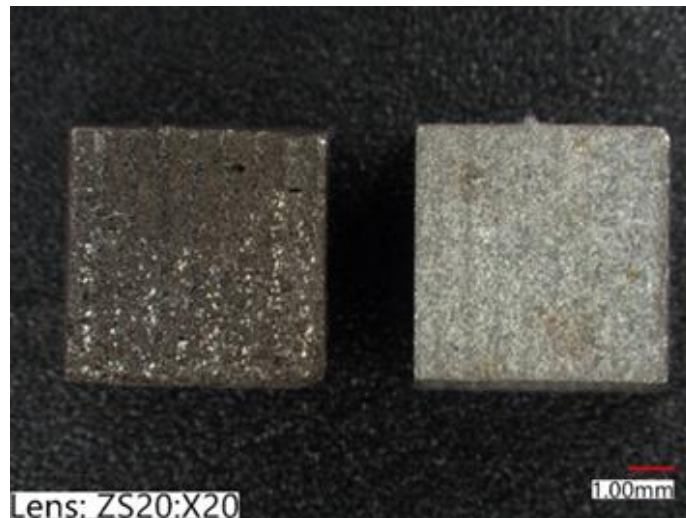


Figure 7. The as-received AlCuNiMn and AlCuNiMnSi samples from Plasmaterials, Inc.

Table 3. Chemical compositions of the principal elements of the AlCuNiMn and AlCuNiMnSi alloy

<b>As-received non-Si samples (Al-Cu-Ni-Mn)</b>					
<b>Element</b>	<b>Al</b>	<b>Cu</b>	<b>Ni</b>	<b>Mn</b>	<b>Si</b>
<b>As received</b>	24.4	35	19.9	20.7	0
<b>600°C</b>	23.7	35	20.3	21	0
<b>800°C</b>	24.7	31.9	20.5	22.9	0
<b>1000°C</b>	25.4	33.9	23.7	17.1	0
<b>Average</b>	<b>24.55</b>	<b>33.95</b>	<b>21.10</b>	<b>20.43</b>	<b>0</b>
<b>Manufacturer</b>	<b>25</b>	<b>25</b>	<b>25</b>	<b>25</b>	<b>0</b>
<b>As-received High-Entropy Alloys (Al-Cu-Ni-Mn-Si)</b>					
<b>Element</b>	<b>Al</b>	<b>Cu</b>	<b>Ni</b>	<b>Mn</b>	<b>Si</b>
<b>As received</b>	17.1	20.3	20.7	20	21.9
<b>600°C</b>	17	23.8	18	19.4	21.9
<b>800°C</b>	17.3	23.9	18.1	19.8	20.9
<b>1000°C</b>	17.6	23	18.8	19.4	21.2
<b>Average</b>	<b>17.25</b>	<b>22.75</b>	<b>18.90</b>	<b>19.65</b>	<b>21.45</b>
<b>Manufacturer</b>	<b>20</b>	<b>20</b>	<b>20</b>	<b>20</b>	<b>20</b>

In preparation for annealing treatments, the alloys are placed in cylindrical ceramic crucibles with lids to facilitate temperature control and establish a chemically inert environment. The annealing treatments took place in Sentro Tech High Temperature Box furnaces with ramp up temperature settings of 10°C per minute up to the annealing temperature, held at the annealing temperature for 24 hours in air, then cooled at the same rate of 10°C per minute to room temperature. This is repeated for 600, 800 and 1000°C temperatures for each alloy.

### 3.2 MICROSTRUCTURE, CHEMICAL, AND STRUCTURAL CHARACTERIZATION

The microstructures and composition of the sample surfaces are characterized for each of these experimental processes:

- The initial microstructures for both groups of specimens are established before annealing.

- After annealing, the surfaces of the specimens are again ground to observe the bulk microstructural changes.
- After corrosion testing, the surfaces are characterized to document the effects of corrosion testing on each surface.

The surfaces are characterized using a Hitachi SU 3500 Scanning Electron Microscope (SEM) operating in backscattered electron (BSE) and secondary electron (SE) mode at 10-15 kV. Energy Dispersive Spectroscopy (EDS, Oxford Instruments), attached to the Hitachi SU 3500 system, is used to identify the primary constituents, determine any chemical compositional changes, and assist in identifying oxidation formation and corrosion products. The composition of possible oxide formation is identified using X-ray Diffraction (XRD, Bruker D8 Discover) with  $\text{CuK}\alpha$  radiation. XRD operation parameters for each sample include a 4 hour scan, applied voltage of 40 kV voltage, current of 30 mA applied to the x-ray tube, and  $2\theta$  values ranging from  $10^\circ$  to  $100^\circ$ .

### **3.3 ELECTROCHEMICAL CORROSION EXPERIMENTATION**

Prior to corrosion testing, each sample is ground on one surface of the cube using 400, 600, and 1200 grit SiC paper. A small hole is drilled into one of the unground side surfaces, then a 4-inch PVC-insulated copper wire is electrically connected upon insertion into the hole. Hot glue is poured over the drilled hole, around the exposed copper wire, and around five of the six cube sides, leaving only the ground surface exposed. A Gamry Potentiostat (Interface 1010E) and a typical three-electrode cell is used to run the corrosion tests. The corrosion cell set-up includes a graphite electrode counter electrode, an Ag/AgCl reference electrode and the test specimen (with an approximately sample area of  $0.25 \text{ cm}^2$ ) as the working electrode. All electrochemical corrosion measurements are performed in 3.5 wt% NaCl solution at room temperature. Three

electrochemical tests procedures are executed using the Gamry Framework and analyzed with the Gamry Echem Analyst software:

- Open circuit potential (OCP) is stabilized for 600 seconds (10 minutes) to obtain a relatively stable signal.
- Linear polarization resistance to determine the corrosion rate.
- The potentiodynamic scan is performed at a scan rate of 1 mV/s.

Calibrations are conducted in compliance with the ASTM standards G5, G59, and G61.

Each test is repeated three times and the two tests with the closest values are reported.

## **4. Results**

### **4.1 MICROSTRUCTURES OF AS-RECEIVED ALLOYS**

#### **4.1.1 Microstructures of As-received AlCuNiMn Alloy**

The microstructure and XRD pattern of the as-received AlCuNiMn alloy are presented in Figures 8 and 9. The constituent phase or microconstituent is identified by comparing the contrast and chemical compositional differences for each EDS scan (as illustrated by comparing Figures 8a and 8b). The AlCuNiMn alloy contains a dendritic structure with two solid solutions and one ternary constituent. Ni-rich (white regions), Mn-rich (black regions), and a AlCuMn-rich (gray regions) microconstituents are visible in the micrographs. Coring is present around the Ni-rich area, indicative of the as-received structure, where the center of the grain is Ni-rich (as it has the highest-melting temperature compared to the other elements), and the Mn content (one of the lowest-melting elements) increases around the grain boundary. Mn is the first to oxidize upon solidification as it sits in the inter-dendritic regions or grain boundaries. The AlCuMn-rich region lies between the Ni-rich and Mn-rich regions. An interfacial separation is detected between the Ni solid solution and the ternary (AlCuMn-rich) constituent. XRD analysis (Figure 9) confirms

the data regarding the three distinct regions, gathered through EDS. The peaks are labeled, where the AlCuMn-rich (gray) microconstituent is represented by the red lines (and red ▲ symbol) with a stoichiometry of  $Al_{3.892}Cu_{6.10808}$ , the Ni regions are labeled with the smaller pink lines (pink ▲ symbol), and the Mn-rich (black) constituent phase is identified with the blue lines (▼ blue symbol).

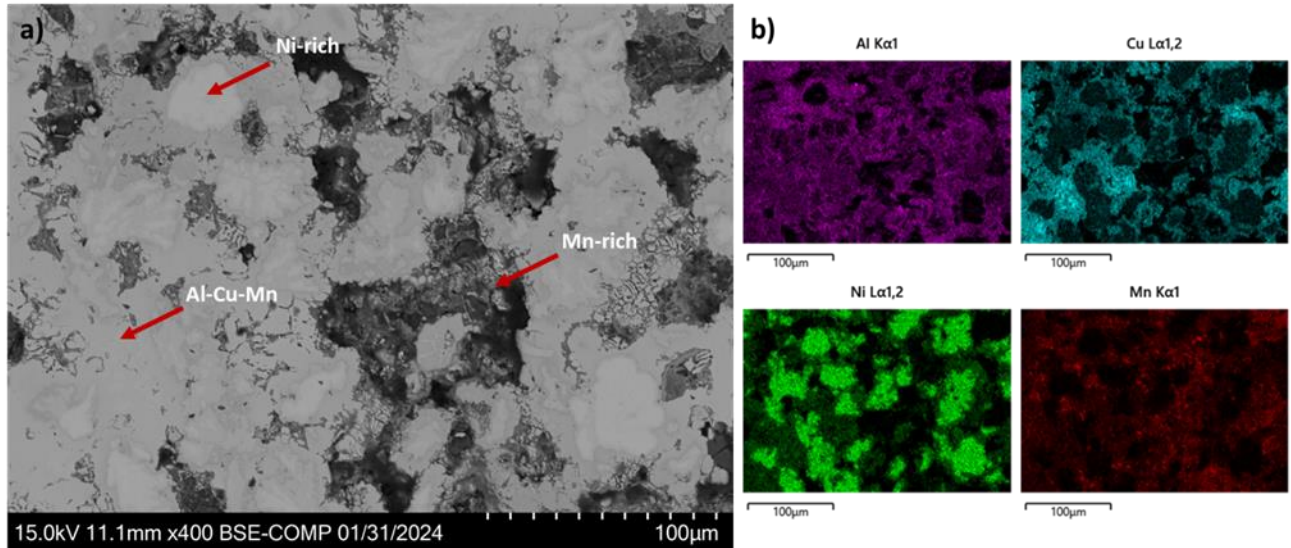


Figure 8. Microstructures of the as-received AlCuNiMn with (a) SEM image in BSE mode, and (b) EDS scans for each element.

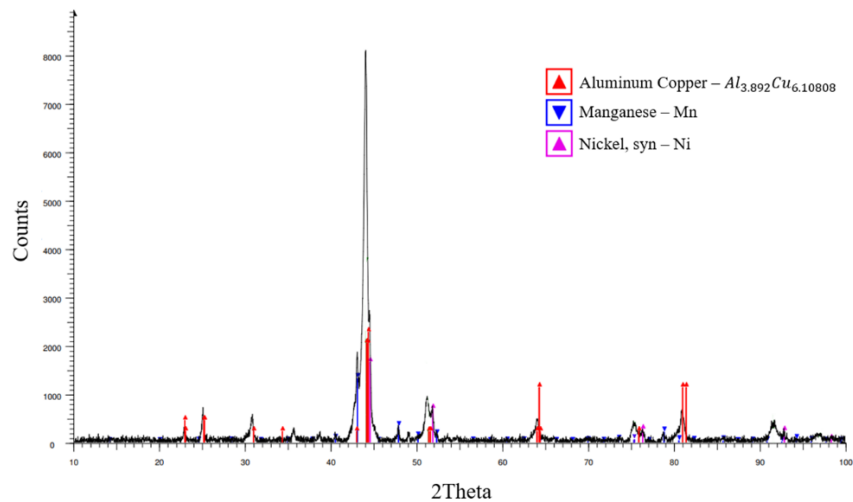


Figure 9. XRD pattern of the as-received AlCuNiMn alloy.

#### 4.1.2 Microstructures of As-received AlCuNiMnSi Alloy

The microstructure and XRD pattern of the as-received AlCuNiMnSi alloy are presented in Figures 10 and 11. The addition of a fifth alloying element, silicon, leads to the redistribution of the other elements and the evolution of a fourth constituent phase. The microstructure consists of a dendritic structure with one solid solution constituent phase, two binary constituent phases, and one ternary constituent phase. The white region is still Ni-rich, however, the gray and black regions are replaced with AlCuNi-rich (gray) and AlMn-rich (black) constituents, respectively. The new dark gray patchy region is MnSi-rich. Coring is also identifiable in the AlCuNiMnSi alloy where the center of the white grain is Ni-rich and the content of both the lowest melting elements, Al and Mn, increases from this area toward the inter-dendritic regions. An interfacial separation is detected between the Ni-rich and AlCuNi-rich regions, similar to AlCuNiMn. XRD analysis of the AlCuNiMnSi alloy confirms the existence of both the Ni (white) and AlCuNi-rich (gray) regions, where the latter is represented with an  $Al_{3.892}Cu_{6.10808}$  stoichiometry, similar to the Al-Cu-Mn region in the AlCuNiMn alloy. The presence of a Mn-Si rich region is represented by  $Mn_5Si_3$ . XRD did not identify the AlMn-rich region but included a NiAl-peak corresponding to a  $Ni_{0.92}Al_{1.05}$  stoichiometry, which may be from the interfacial separation or region surrounding the Ni phase. The peaks are labeled, where the AlCuNi-rich (gray) region is represented by the red lines (and red ▲ symbol) with a stoichiometry of  $Al_{3.892}Cu_{6.10808}$ , the Ni regions are labeled with pink lines (pink ▲ symbol), the MnSi-rich (dark gray patchy) region is identified with the green lines (green ⚡ symbol), and the NiAl-rich region is represented by the blue lines (blue ▼ symbol).

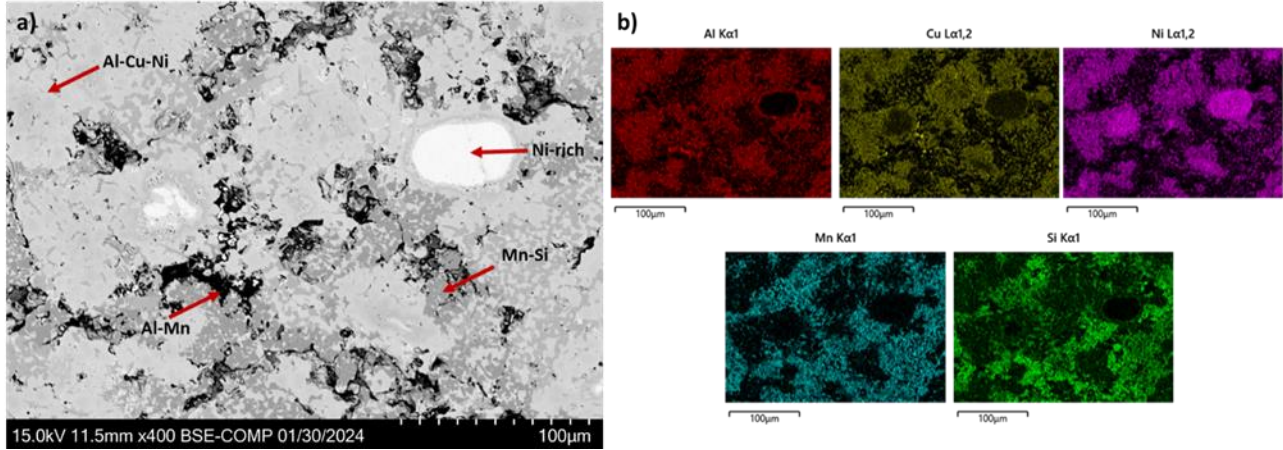


Figure 10. Microstructure of the as-received condition of the AlCuNiMnSi with (a) SEM image in BSE mode and (b) EDS scans for each individual element.

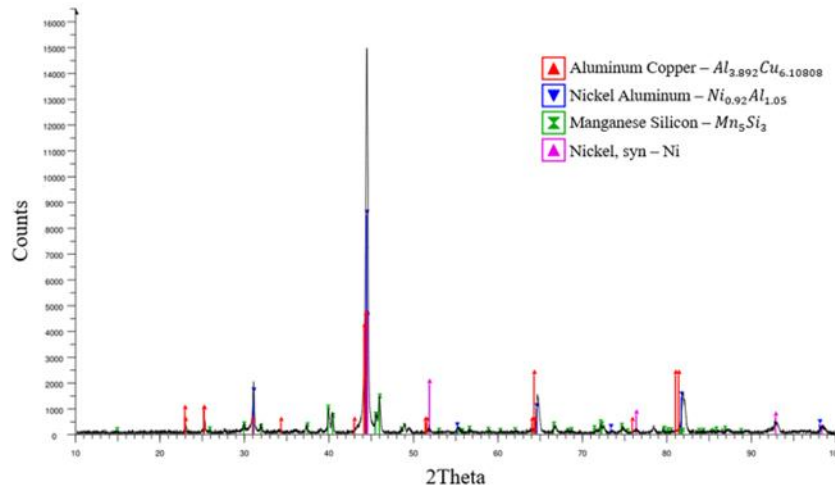


Figure 11. XRD pattern of the as-received AlCuNiMn alloy.

### 4.1.3 Comparison of As-received AlCuNiMn and AlCuNiMnSi Alloys

The surfaces of the AlCuNiMn and AlCuNiMnSi alloys are compared in this section using surface topography and elemental analysis of the constituent phases in each alloy. SEM imaging in backscattered electron (BSE) and secondary electron (SE) mode reveal that the black regions present in both alloys (Figures 8 and 10) are actually casting defects, specifically voids. Figure 12 is a comparison between the two materials illustrating that the addition of Si to the AlCuNiMn decreases the size and depth of these voids.

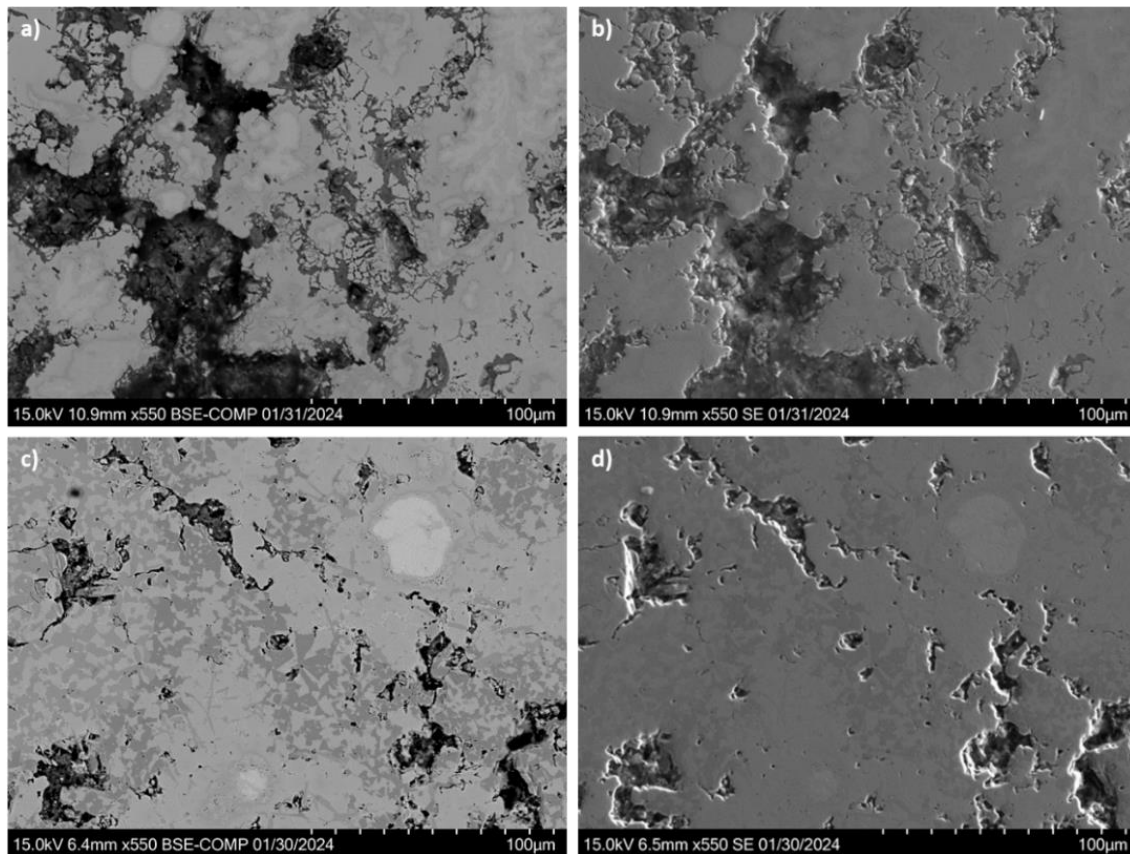


Figure 12. SEM images of the microstructures of the as received AlCuNiMn alloy in (a) BSE mode and (b) SE mode; and the AlCuNiMnSi in (c) BSE mode and (d) SE mode.

The average composition of each alloy constituent phase is summarized in Table 4. Note that the average composition is determined by averaging four different areas. Table 4 illustrates the relative changes in composition of each constituent. Based on the data, a clear distinction is observed for each region, that results in the identification of three constituents for the AlCuNiMn alloy and four constituents for the AlCuNiMnSi alloy. Note that the AlMn-rich area is not identified by XRD analysis, but that XRD did identify an AlNi-rich area. As mentioned above, it is possible that the AlNi peak is from the regions surrounding the Ni-rich areas as Al is identified in these areas from the EDS mapping (see Figure 10). It is also possible that the AlMn-rich area is a disordered structure that is not identifiable by XRD.

Table 4. Summary of the constituent phase compositions in AlCuNiMn and AlCuNiMnSi.

Medium-Entropy Alloy (AlCuNiMn)			High-Entropy Alloy (AlCuNiMnSi)		
Phases	Elements	At%	Phases	Elements	At%
Aluminum-Copper-Manganese rich	Al	24.75	Aluminum-Copper-Nickel rich	Al	34.04
	Cu	40.95		Cu	27.41
	Ni	11.70		Ni	26.72
	Mn	22.55		Mn	3.54
	Si	0		Si	8.24
Nickel rich	Al	3.45	Nickel-rich	Al	0.77
	Cu	2.22		Cu	0.15
	Ni	92.54		Ni	97.97
	Mn	1.80		Mn	0.71
	Si	0		Si	0.40
Manganese rich	Al	8.88	Aluminum-Manganese rich	Al	42.25
	Cu	16.07		Cu	7.88
	Ni	11.79		Ni	4.82
	Mn	63.24		Mn	35.02
	Si	0		Si	10.01
			Manganese-Silicon rich	Al	2.20
				Cu	1.99
				Ni	4.70
				Mn	44.99
				Si	46.12

## 4.2 OXIDATION FORMATION AND MICROSTRUCTURAL EVOLUTION FROM HEAT

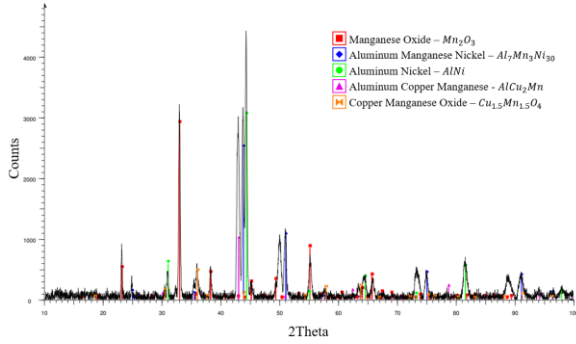
### TREATMENT PROCESS

#### 4.2.1 Oxide Formation in AlCuNiMn and AlCuNiMnSi

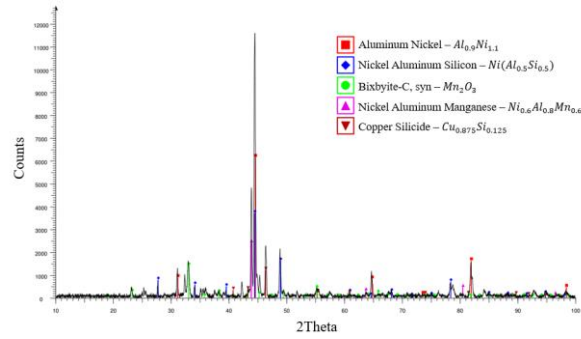
The AlCuNiMn and AlCuNiMnSi alloys are both heat treated at 600°C, 800°C, and 1000°C for 24 hours in air. The XRD results at each temperature for both alloys are shown in Figure 13 and summarized in Table 5. The first oxide to appear after annealing at temperatures of 600°C and 800°C in both alloys is  $Mn_2O_3$ , also referred to as bixbyite. This specific oxide formation at these temperatures have already been reported by Hitter et al. [50] after annealing at 600°C, 700°C, and 800°C. The AlCuNiMn forms  $Cu_xMn_yO_4$ , with varying x and y values after

annealing at 600°C and 800°C. The Mn oxide transitions to  $Mn_3O_4$  and  $Cu_4O_3$  with no other oxides present after annealing at 1000°C. The AlCuNiMnSi alloy forms  $(NiO)_{0.5}(MnO)_{0.5}$  and  $Al_2O_3$  after annealing at 800°C and 1000°C,  $Ni_{6.8}Mn_{0.6}O_8$  after annealing at 800°C, and  $Cu_{1.4}Mn_{1.6}O_4$  at after annealing at 1000°C.

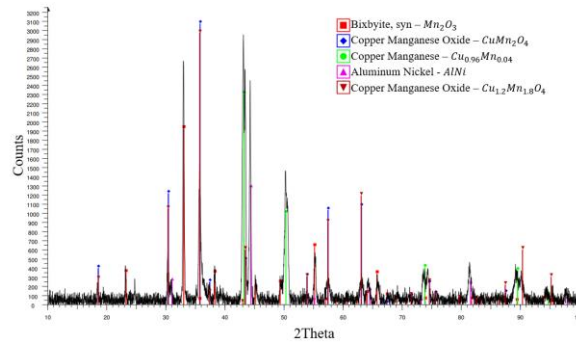
(a) Non-Si (AlCuNiMn) at 600°C



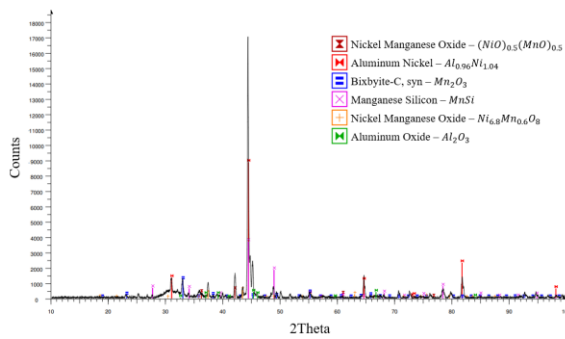
(d) Si alloy (AlCuNiMnSi) at 600°C



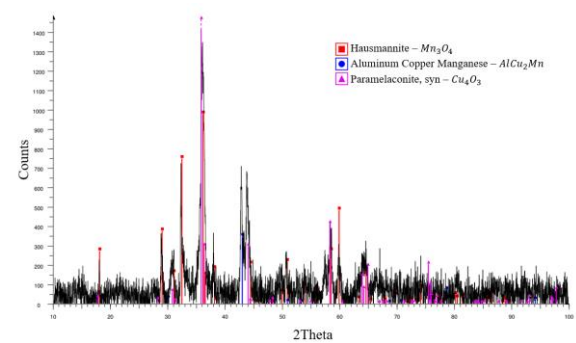
(b) Non-Si (AlCuNiMn) at 800°C



(e) Si alloy (AlCuNiMnSi) at 800°C



(c) Non-Si (AlCuNiMn) at 1000°C



(f) Si alloy (AlCuNiMnSi) at 1000°C

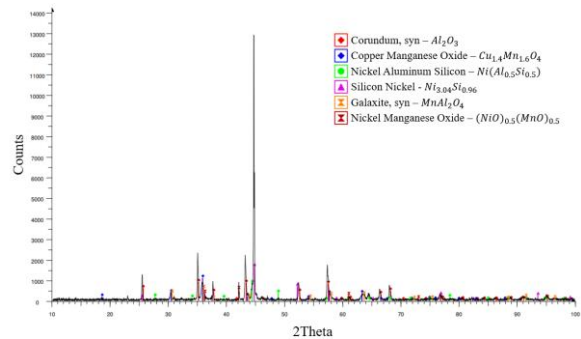


Figure 13. XRD results showing oxide formations of the AlCuNiMn alloy at (a) 600°C, (b) 800°C, and (c) 1000°C, and the AlCuNiMnSi alloy at (d) 600°C, (e) 800°C, and (f) 1000°C.

Table 5. Summary of the oxides identified with XRD for each alloy in its respective annealing temperature.

AlCuNiMn		
600°C	800°C	1000°C
Mn <sub>2</sub> O <sub>3</sub> Cu <sub>1.5</sub> Mn <sub>1.5</sub> O <sub>4</sub>	Mn <sub>2</sub> O <sub>3</sub> Cu <sub>1.2</sub> Mn <sub>1.8</sub> O <sub>4</sub> CuMn <sub>2</sub> O <sub>4</sub>	Mn <sub>3</sub> O <sub>4</sub> Cu <sub>4</sub> O <sub>3</sub>
AlCuNiMnSi		
600°C	800°C	1000°C
Mn <sub>2</sub> O <sub>3</sub>	Mn <sub>2</sub> O <sub>3</sub> (NiO) <sub>0.5</sub> (MnO) <sub>0.5</sub> Ni <sub>6.8</sub> Mn <sub>0.6</sub> O <sub>8</sub> Al <sub>2</sub> O <sub>3</sub>	MnAl <sub>2</sub> O <sub>4</sub> (NiO) <sub>0.5</sub> (MnO) <sub>0.5</sub>  Al <sub>2</sub> O <sub>3</sub> Cu <sub>1.4</sub> Mn <sub>1.6</sub> O <sub>4</sub>

#### 4.2.2 Microstructural Evolution of AlCuNiMn

Table 6 summarizes the microstructural evolution for the as-received and annealed AlCuNiMn samples (at temperatures of 600°C, 800°C, and 1000°C). The types of microconstituents and their composition are reported. The microconstituents that are eliminated, and new phases which evolve as the oxidation temperature is increased are described in detail below.

##### As-received AlCuNiMn Sample

As previously mentioned, the microstructure of the as-received AlCuNiMn sample is a dendritic structure containing two solid solution constituent phases (Ni and Mn) and one ternary constituent phase (AlCuMn).

Table 6. The phase composition of AlCuNiMn alloy at various annealing temperatures as identified by EDS

Non-Si as received			Non-Si at 600°C			Non-Si at 800°C			Non-Si at 1000°C				
Phases	Element	AT%	Phases	Element	AT%	Phases	Element	AT%	Phases	Element	AT%		
Nickel-rich	Al	3.45	Nickel-rich	Al	2.78								
	Cu	2.22		Cu	1.70								
	Ni	92.54		Ni	92.56								
	Mn	1.80		Mn	2.98								
Aluminum-Copper-Manganese	Al	24.75	Aluminum-Copper-Manganese	Al	22.25								
	Cu	40.95		Cu	52.38								
	Ni	11.70		Ni	8.10								
	Mn	22.55		Mn	17.27								
Manganese-rich	Al	8.88	Manganese-rich	Al	2.65	Manganese-rich	Al	10.42					
	Cu	16.07		Cu	0.92		Cu	4.60					
	Ni	11.79		Ni	0.57		Ni	1.27					
	Mn	63.24		Mn	95.88		Mn	83.71					
			Aluminum-Copper-Nickel-Manganese	Al	39.04	Aluminum-Copper-Nickel-Manganese	Al	26.99	Aluminum-Copper-Nickel-Manganese	Al	16.86		
				Cu	9.19		Cu	14.36		Cu	23.70		
				Ni	41.33		Ni	43.91		Ni	34.38		
				Mn	10.48		Mn	14.73		Mn	25.07		
						Copper-Nickel-Manganese	Al	6.94	Copper-Nickel-Manganese	Al	4.26		
							Cu	73.00		Cu	52.21		
							Ni	10.69		Ni	19.45		
							Mn	9.39		Mn	24.06		
									Aluminum-rich	Al	86.71		
										Cu	9.96	Cu	9.96
										Ni	0.73	Ni	0.73
										Mn	2.60	Mn	2.60

#### AlCuNiMn Sample Annealed at 600°C

The microstructure of the AlCuNiMn sample annealed at 600°C for 24 hours is shown in Figure 14 with corresponding EDS mapping of each individual element. Annealing causes a fourth constituent phase to emerge within the inter-dendritic grain structure, a quaternary (AlCuNiMn-rich) microconstituent appears, depicted by the darker gray cloudy areas. With the appearance of this phase, the Ni-rich is present in smaller proportions throughout the microstructure.

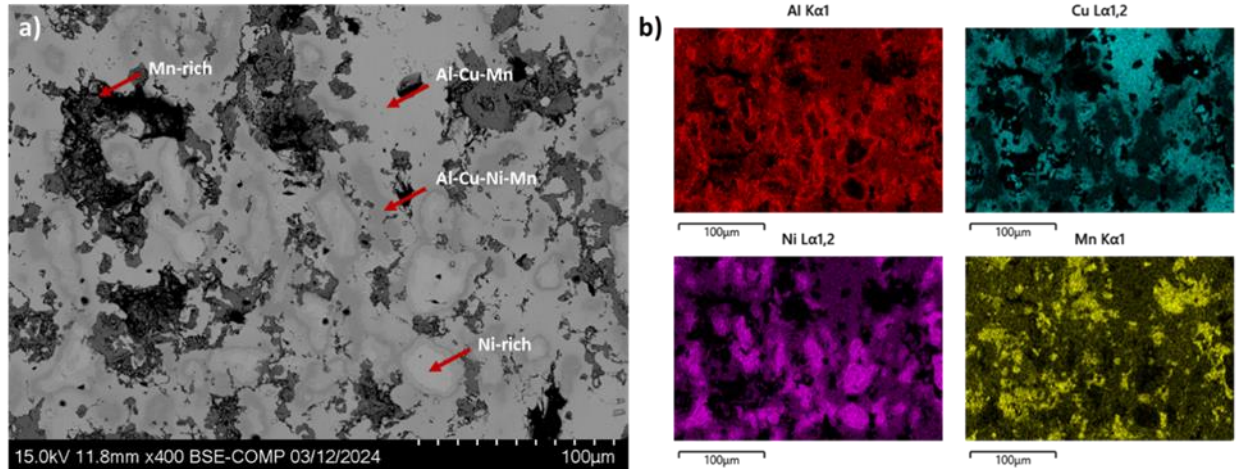


Figure 14. Microstructure of the AlCuNiMn sample annealed at 600°C with (a) SEM image in BSE mode and (b) EDS scans for each individual element.

#### AlCuNiMn Sample Annealed at 800°C

Figure 15 includes the microstructure of the AlCuNiMn sample annealed at 800°C for 24 hours in air with corresponding EDS mapping of each individual element. The Ni solid solution constituent phase and the ternary (AlCuNi-rich) constituent phase are no longer detected after this annealing treatment. However, the quaternary (AlCuNiMn-rich) microconstituent introduced at 600°C increases in quantity throughout the microstructure. The appearance of a new ternary constituent phase (CuNiMn-rich) is also present. Within the inter-dendritic grain structure, two constituent phases are observed: the quaternary and newly formed ternary (CuNiMn-rich) phase. It also appears that the Al content increases within some of the inter-dendritic regions, but not enough to overpower the predominately Mn content. Within those regions, the oxide filled regions are identified to be a combination of  $Mn_2O_3$  and some variation of  $Cu_xMn_yO_4$ . Not much pull out is seen in this microstructure and the number of voids appear to decrease.

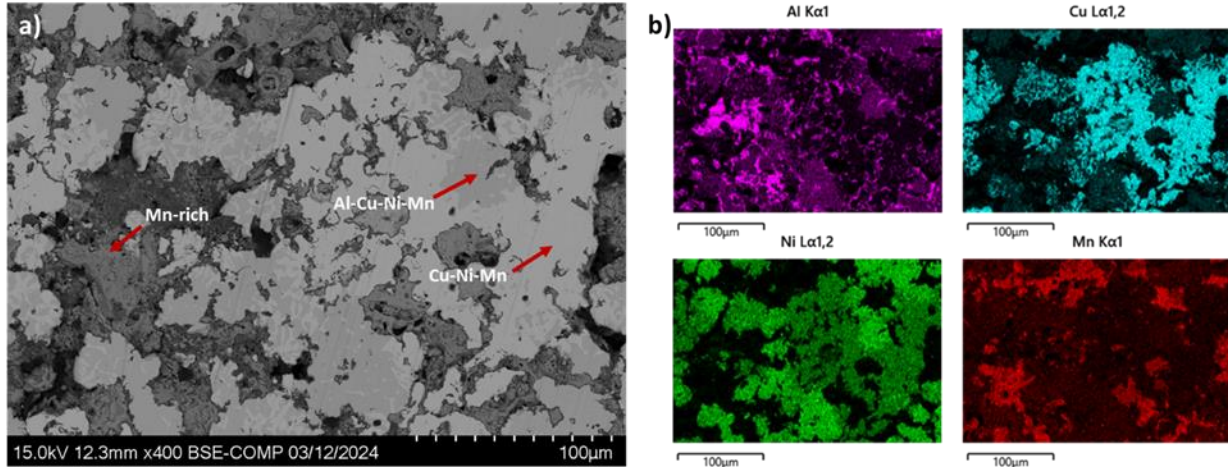


Figure 15. Microstructure of the AlCuNiMn sample annealed at 800°C with (a) SEM image in BSE mode and (b) EDS scans for each individual element.

#### AlCuNiMn Sample Annealed at 1000°C

Figure 16 includes a SEM image of the microstructure after annealing at 1000°C, along with EDS elemental mapping. With an increase in annealing temperature from 800°C to 1000°C, the darker contrast inter-dendritic regions transition from Mn rich to Al rich. The branches of these regions become thinner in size. The number and size of the voids within the film decrease in this sample. Within the inter-dendritic grain structure, the AlCuNiMn-rich regions expand compared to the samples with lower annealing temperatures and contain a higher Ni content compared to the other constituent phases. The lighter gray regions surrounding the AlCuNiMn-rich areas are CuNiMn-rich, that persists in all samples, starting with the as-received sample and through all annealing temperatures. The grain boundaries surrounding the AlCuNiMn/CuNiMn regions are Al-rich. It appears that the oxides detected by XRD,  $Mn_3O_4$  and  $Cu_4O_3$ , are present in the Al-rich region as identified by XRD.

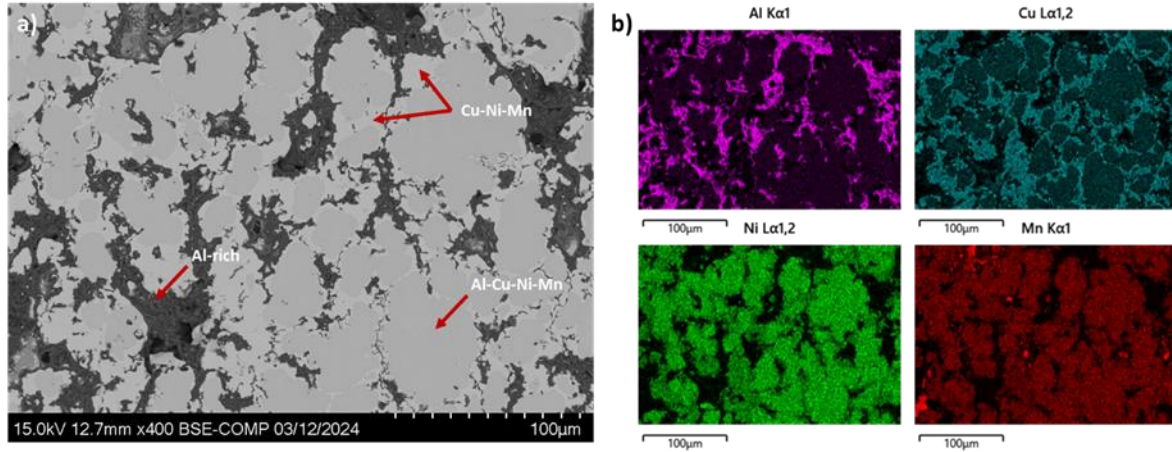


Figure 16. Microstructure of the AlCuNiMn sample annealed at 1000°C with (a) SEM image in BSE mode and (b) EDS scans for each individual element.

### Summary of the AlCuNiMn alloy microstructural evolution

When the AlCuNiMn sample is annealed at 600°C, the total number of constituents increases from three to four, as the quaternary (AlCuNiMn-rich) constituent is introduced. This constituent is also present at annealing temperatures of 800°C and 1000°C, however, its composition evolves with temperature, where Cu and Mn increase at the expense of Al and Ni until at 1000°C, where Cu, Ni and Mn are almost equal. Annealing at 800°C eliminates both the Ni-rich and the AlCuMn-rich constituents and a CuNiMn-rich constituent appears. Annealing at 1000°C eliminates the Mn-rich regions, maintains the AlCuNiMn and CuNiMn constituents, and introduces an Al-rich region. As with the AlCuNiMn constituent, the CuNiMn-rich constituent becomes more homogeneous with increase in annealing temperature up to 1000°C. The Al content in both these constituents decreases and contributes to the formation of the Al-rich phase. There is a visible transition of two phases trying to emerge as one (the AlCuNiMn-rich and the CuNiMn-rich). The constituent phases present after annealing at 1000°C can also be characterized by their aluminum content, with low (< 5%), medium (~20%), and high (>80%) Al concentrations. With increasing temperature, diffusion is occurring leading to mobility of the

atoms. That mobility causes changes within the structure. In summary, the annealing treatment is providing a more organized and behaved structure compared to the as-received condition. As the annealing temperature of the AlCuNiMn alloy is increased to 1000°C, the microstructure transitions to a more uniform structure compared to the as-received AlCuNiMn alloy and the corresponding samples annealed at 600°C and 800°C. This is visualized in Figure 17, which contains SEM images in BSE mode along with SEM images in SE mode for 600°C and 1000°C annealed samples to provide better visualization for observation analysis. Annealing causes the void size to decrease and not much pull out from the oxidation experimentation is present on the surface. It appears that increasing the annealing temperature, not only decreases the size of the voids but reduces their depth as well.

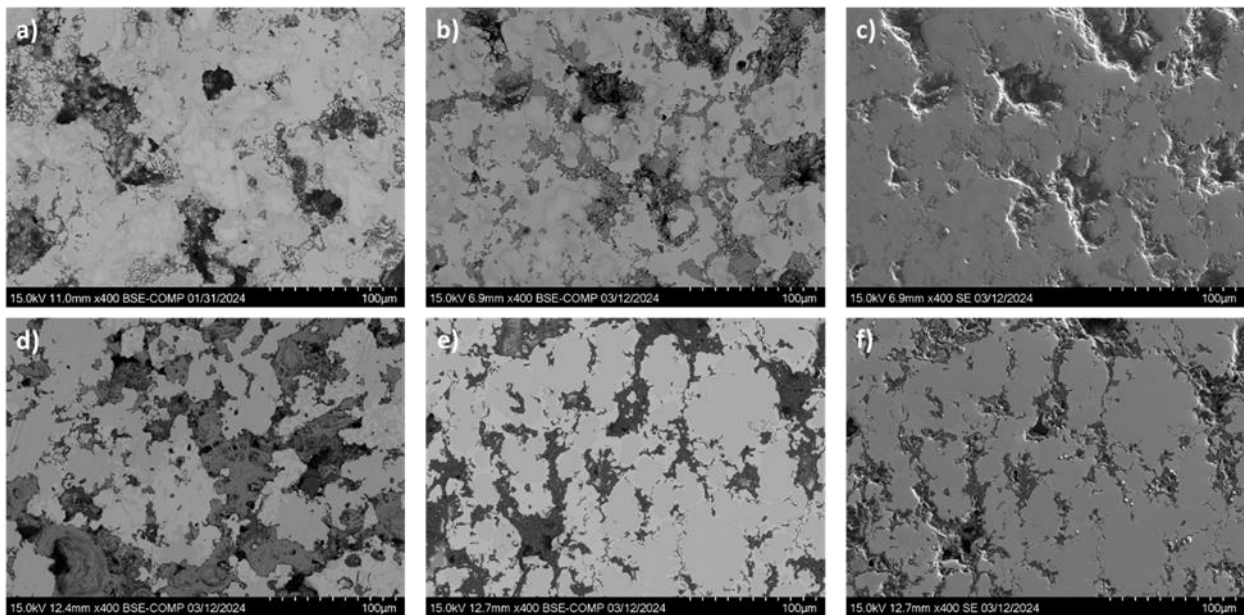


Figure 17. SEM images of the AlCuNiMn alloy in the (a) as received condition and (b-c) annealed at 600°C in BSE and SE mode, (d) 800°C, and (e-f) 1000°C in BSE and SE mode.

### 4.2.3 Microstructure Evolution of AlCuNiMnSi

Table 7 summarizes the microstructural evolution for the as-received and annealed AlCuNiMnSi samples (at temperatures of 600°C, 800°C, and 1000°C). The types of microconstituents and their composition are reported. The microconstituents that are eliminated, and new constituent phases which evolve as the oxidation temperature is increased are described in detail below.

#### As-received AlCuNiMnSi Sample

The microstructure of the AlCuNiMnSi alloy in the as-received condition is a dendritic structure containing one solid solution phase (Ni-rich), two binary phases (AlMn- and MnSi-rich), and one ternary phase (AlCuNi-rich).

Table 7. The phase composition of AlCuNiMnSi alloy at various annealing temperatures as identified by EDS

Si Alloy as received			Si Alloy at 600°C			Si Alloy at 800°C			Si Alloy at 1000°C				
Phases	Element	AT%	Phases	Element	AT%	Phases	Element	AT%	Phases	Element	AT%		
Nickel rich	Al	0.77	Nickel rich	Al	0.67								
	Cu	0.15		Cu	1.50								
	Ni	97.97		Ni	96.05								
	Mn	0.71		Mn	1.05								
	Si	0.40		Si	0.72								
Aluminum-Manganese rich	Al	42.25	Aluminum-Manganese rich	Al	21.56	Aluminum-Manganese rich	Al	59.14					
	Cu	7.88		Cu	2.56		Cu	3.72					
	Ni	4.82		Ni	3.76		Ni	1.50					
	Mn	35.02		Mn	69.92		Mn	31.54					
	Si	10.01		Si	2.24		Si	4.12					
Manganese-Silicon rich	Al	2.20	Manganese-Silicon rich	Al	0.90	Manganese-Silicon rich	Al	1.58	Manganese-Silicon rich	Al	0.33		
	Cu	1.99		Cu	1.66		Cu	1.58		Cu	1.58		
	Ni	4.70		Ni	5.96		Ni	4.68		Ni	8.70		
	Mn	44.99		Mn	50.65		Mn	44.75		Mn	55.63		
	Si	46.12		Si	40.81		Si	47.41		Si	33.80		
Aluminum-Copper-Nickel rich	Al	34.04	Aluminum-Copper-Nickel rich	Al	33.80	Aluminum-Copper-Nickel rich	Al	30.01	Aluminum-Copper-Nickel rich	Al	22.70		
	Cu	27.41		Cu	24.28		Cu	34.16		Cu	38.25		
	Ni	26.72		Ni	33.14		Ni	26.86		Ni	28.88		
	Mn	3.54		Mn	1.42		Mn	1.44		Mn	1.11		
	Si	8.24		Si	7.34		Si	7.57		Si	9.07		
			Copper-Nickel-Manganese-Silicon rich	Al	6.27	Copper-Nickel-Manganese-Silicon rich	Al	2.74	Copper-Nickel-Manganese-Silicon rich	Al	2.8		
				Cu	38.30		Cu	16.2		Cu	13.54		
				Ni	18.33		Ni	25.99		Ni	31.66		
				Mn	15.50		Mn	29.24		Mn	29.14		
				Si	21.67		Si	25.84		Si	22.88		
									Copper-Nickel-Silicon rich	Al	7.00		
										Cu	60.34	Cu	60.34
										Ni	17.37	Ni	17.37
										Mn	0.77	Mn	0.77

				Si	14.51
			Nickel- Manganese- Silicon rich	Al	2.8
				Cu	1.32
				Ni	20.26
				Mn	33.56
				Si	42.02

### AlCuNiMnSi Sample Annealed at 600°C

The microstructure along with EDS mapping of the individual elements for the AlCuNiMnSi sample annealed at 600°C for 24 hours in air is shown in Figure 18. The microconstituents presented in the as-received sample are all found in the annealed sample at 600°C. As is the case with the AlCuNiMn alloy, a quaternary (CuNiMnSi-rich) microconstituent also appears, for a total of five constituents. This phase is presented in small quantities around the edges of the inter-dendritic regions or Al-Mn rich constituent phase. The Ni-rich phase is now only found in small amounts or volume fraction of the microstructure (Figure 23). However, the interfacial separation between the Ni-rich and AlCuNi-rich constituents appears to be a wider compared to the sample in the as-received condition. The oxide within the inter-dendritic regions is  $Mn_2O_3$ . The microstructure has similar characteristics as the AlCuNiMn sample annealed at 600°C (as seen in Figure 14).

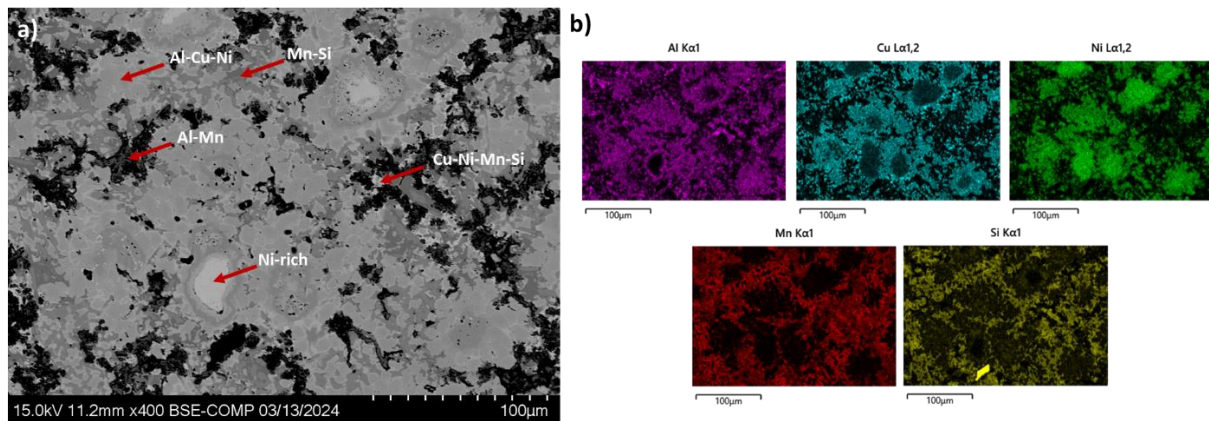


Figure 18. Microstructure of the AlCuNiMnSi sample annealed at 600°C with (a) SEM image in BSE mode and (b) EDS scans for each individual element.

### AlCuNiMnSi Sample Annealed at 800°C

The microstructure developed after annealing the AlCuNiMnSi sample at 800°C for 24 hours in air is shown in Figure 19. Some notable features include the elimination of the Ni-rich solid solution constituent phase and the increase volume fraction of the quaternary (CuNiMnSi-rich) constituent phase. The Mn-Si rich microconstituent is depleting in proportions throughout the microstructure due to Si also becoming rich in other constituents. The inter-dendritic regions or grain boundaries appear to be more dispersed as each grain is more easily identified. The size of the boundaries is thinner compared to similar regions for the annealed AlCuNiMnSi sample at 600°C. Due to the absence of the Ni-rich microconstituent, the AlCuNi-rich ternary constituent blends into the quaternary (CuNiMnSi-rich) region followed by the Mn-Si binary phase then lastly the AlMn-rich constituent that sits within the inter-dendritic regions or grain boundaries.

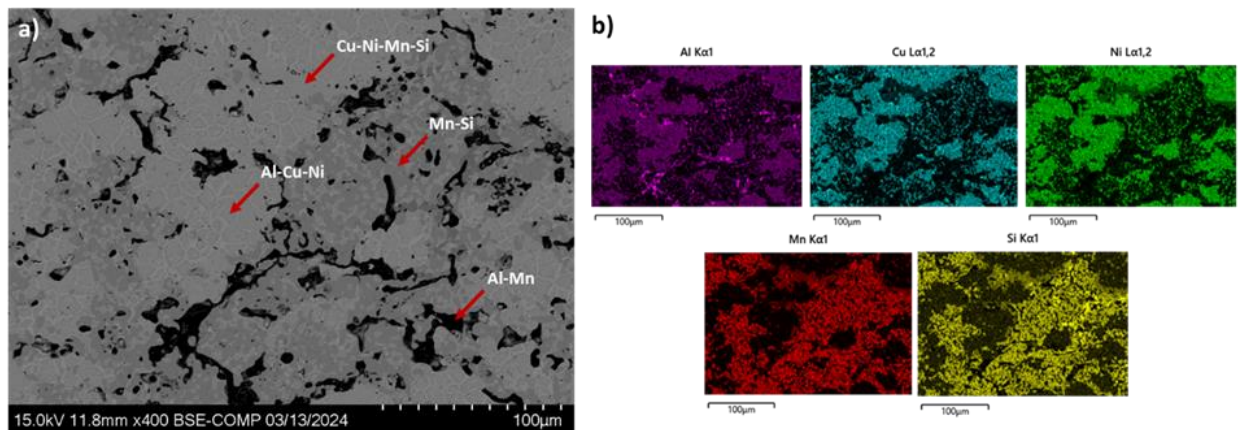


Figure 19. Microstructure of the AlCuNiMnSi sample annealed at 800°C with (a) SEM image in BSE mode and (b) EDS scans for each individual element.

### AlCuNiMnSi Sample Annealed at 1000°C

The AlCuNiMnSi sample annealed at 1000°C yielded an unexpected result and thus, will only be analyzed in this section and is not included in the corrosion study. It has yet to be

determined what took place during the heat treatment process as there are no phase diagrams available for this AlCuNiMnSi system. From observation alone, it is suggested or concluded that the AlCuNiMnSi sample began to oxidize during heat treatment and during the temperature increase or when the temperature reached 1000°C, the alloy reached its melting point. The core of the cube sample melted and found a weak point within its oxidized cube surface to pour out and resolidify on the side of the sample as illustrated in Figure 20. A second AlCuNiMnSi sample annealed at 1000°C to ensure repeatability, and the sample once again melted out of the oxidized cube surface.



Figure 20. AlCuNiMnSi alloy after heat treatment at 1000°C for trials #1 and #2 showing inner contents escaping from oxidized cube exterior.

The microstructure of the AlCuNiMnSi alloy annealed at 1000°C does not resemble any of the other microstructures of the as-received or annealed samples, for either the AlCuNiMn or AlCuNiMnSi alloys. The microstructure of the annealed sample at 1000°C AlCuNiMnSi is shown in Figure 21 at 200x magnification. This annealed alloy consists of different forms of dendritic structures. Due to its complexity and the fact that it is no longer the same alloy it once was, corrosion testing will not be conducted on this specimen.

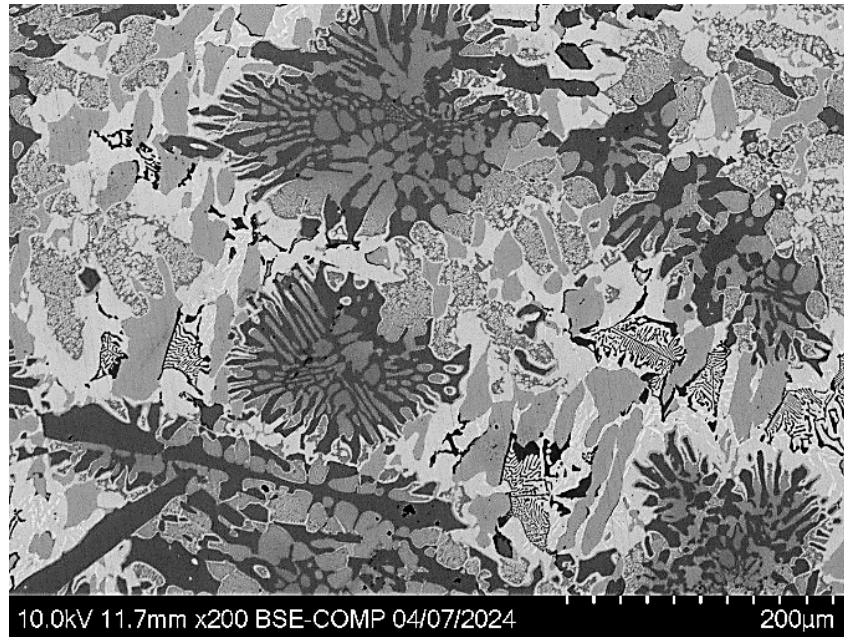


Figure 21. Microstructure of the AlCuNiMnSi sample annealed at 1000°C.

Figure 22 includes images of the microstructure of the same AlCuNiMnSi sample at 400x magnification along with EDS scans of each individual element. Average point ID measurements identify the chemical composition for each microconstituent and are listed in Table 8. The same constituent phases identified in the AlCuNiMnSi sample annealed at 800°C (except for the AlMn-rich) are present in this sample, along with two additional ternary (CuNiSi- and NiMnSi-rich) microconstituents. There are two distinct AlCuNi-rich constituents in two distinct regions. The first of those regions (AlCuNi-1) has a higher Cu content compared to the second region (AlCuNi-2), which has a higher Ni content. The NiMnSi-rich ternary microconstituent resembles a lamellar eutectic formation/structure.

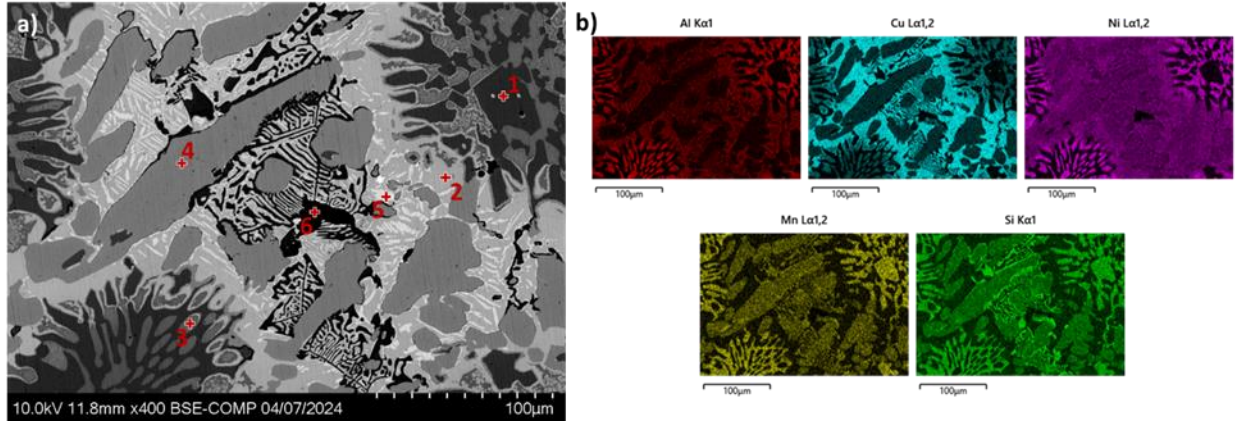


Figure 22. Microstructure of the AlCuNiMnSi sample annealed at 1000°C with (a) SEM image in BSE mode and (b) EDS scans for each individual element.

Table 8. Average Point ID from EDS analysis Table corresponds with Figure 22.

Point 1			Point 2			Point 3		
Region	Element	AT%	Region	Element	AT%	Region	Element	AT%
Mn-Si	Al	0.33	Al-Cu-Ni (1)	Al	18.81	Al-Cu-Ni (2)	Al	26.6
	Cu	1.58		Cu	52.15		Cu	24.35
	Ni	8.7		Ni	18.75		Ni	39.01
	Mn	55.63		Mn	0.78		Mn	1.44
	Si	33.8		Si	9.5		Si	8.64
Point 4			Point 5			Point 6		
Region	Element	AT%	Region	Element	AT%	Region	Element	AT%
Cu-Ni- Mn-Si	Al	2.8	Cu-Ni-Si	Al	7	Ni-Mn-Si	Al	2.8
	Cu	13.54		Cu	60.34		Cu	1.32
	Ni	31.66		Ni	17.37		Ni	20.26
	Mn	29.14		Mn	0.77		Mn	33.56
	Si	22.88		Si	14.51		Si	42.02

Summary of the AlCuNiMnSi alloy microstructural evolution

The binary and ternary constituents resulting from the various annealing temperatures demonstrate that this alloy follows the Hume-Rothery Rules. The Hume-Rothery Rules help predict when a set of elements will form some type of solution. Table 9 summarizes elemental changes in the binary, ternary and quaternary constituent phases for the AlCuNiMnSi sample.

For example, Si replaces Al in the AlMn and MnSi-rich binary constituents. The Al with the largest atomic radius (1.432 Å) gets replaced with Si (1.176 Å), a smaller sized atomic radius element. This is also true for the ternary constituents, where in the AlCuNi- and CuNiSi-rich constituents, the Si (1.176 Å) replaces the Al (1.432 Å). Likewise, the Mn (1.12 Å) replaces the Cu (1.278 Å) in the CuNiSi- and NiMnSi-rich ternary constituent phases. Table 10 summarizes the evolution in chemical composition of the quaternary (CuNiMnSi-rich) constituent as a function of temperature. Increasing the temperature causes the Si concentration to increase (21.67 at% to 25.84 at%), which in turn further depletes the Al (6.27 at% to 2.74 at%) content. The outcome is the same when reviewing the Cu and Mn content in this phase. As Mn becomes richer in content (15.50 at% to 29.24 at%), it pushes out or decreases the Cu content (38.30 at% to 16.20 at%). Cu being a larger atomic radius (1.432 Å) gets replaced by the smallest atomic radius (Mn) of this elemental group (with 1.12 Å).

Table 9. Summary of the elemental phase change in the identified binary and ternary phases of the AlCuNiMn and AlCuNiMnSi alloys.

Elemental Change	Binary Phases				
Si removes Al	Al				Mn
				Si	Mn
Elemental Change	Ternary Phases				
Si removes Al	Al	Cu	Ni		
		Cu	Ni	Si	
Mn removes Cu			Ni	Si	Mn
Elemental Change	Quaternary Phase				
Si removes Al Mn suppresses Cu		Cu	Ni	Si	Mn
Atomic radius:	1.432	1.278	1.243	1.176	1.12

Table 10. Chemical composition of the CuNiMnSi-rich region with increasing annealing temperature.

Quaternary Phase (Cu-Ni-Mn-Si)				
Atomic Radii	Element	600°C	800°C	1000°C
		At%	At%	At%
1.432	Al	6.27	2.74	2.8
1.278	Cu	38.3	16.2	7.43
1.243	Ni	18.33	25.99	25.96
1.12	Mn	15.5	29.24	31.35
1.176	Si	21.67	25.84	32.45

Similar to the AlCuNiMn alloy annealed at 600°C, annealing at 600°C does not eliminate one of the constituents but an additional phase (a quaternary phase CuNiMnSi-rich) to appear in the AlCuNiMnSi alloy, in small quantities. While a AlCuNiMn-rich constituent phase appears in AlCuNiMn alloy, the Al is replaced with the Si in the AlCuNiMnSi alloy. Also, the Ni-rich quantities begin to dwindle then completely dissipate after annealing at 800°C, while the quaternary phase grows. At 1000°C, the AlMn-rich binary constituent is eliminated and two ternary constituents are introduced (CuNiSi and NiMnSi). Throughout the heat treatments for AlCuNiMnSi, the presence of the MnSi-rich and AlCuNi-rich constituents remain. In summary, the microstructure becomes more complex with increasing annealing temperature. The AlCuNiMnSi alloy in both the 600°C and 800°C annealed conditions may cause concern, as after annealing at 600°C, it is composed of 5 phases, and after annealing at 800°C, may have four phases but changes to more complex types of constituent phases. Annealing at 1000°C leads to the formation of a resolidified material consisting of different types of dendritic structures. Figure 23 illustrates the phase transformation for the AlCuNiMnSi alloy in the as-received and annealed (600°C, 800°C, and 1000°C) conditions. Overall, subjecting the alloy to annealing

temperatures does not control the microstructure very well nor does it result in any significant improvement in uniformity.

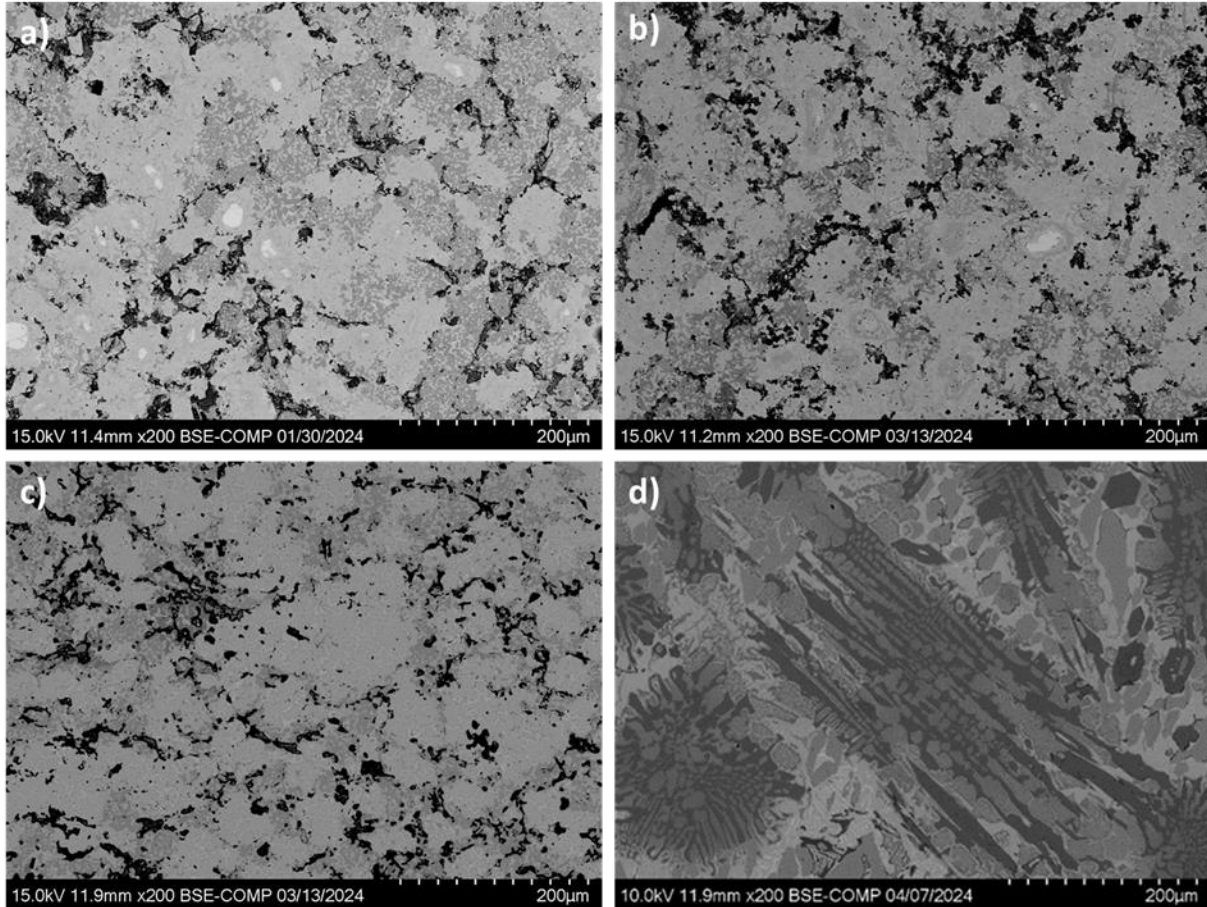


Figure 23. SEM images of the AlCuNiMnSi alloy in the (a) as cast condition and annealed (b) 600°C, (c) 800°C, and (d) 1000°C conditions.

### 4.3 CORROSION BEHAVIOR

The corrosion behavior of the as-received and annealed AlCuNiMn and AlCuNiMnSi alloy specimens in a 3.5% NaCl solution at room temperature is characterized using the potentiodynamic polarization method. The potentiodynamic scans for the AlCuNiMn and AlCuNiMnSi alloys are included in Figures 24 and 32, respectively. The data is graphed as applied potential (E) in volts as a function of current density (i) in A/cm<sup>2</sup>. All potential

measurements are made relative to an Ag/AgCl reference electrode. The Gamry corrosion software reports the corrosion potential ( $E_{\text{corr}}$ ), corrosion current density ( $i_{\text{corr}}$ ), polarization resistance ( $R_p$ ), and corrosion rate in mils per year. Materials with a more positive  $E_{\text{corr}}$  value coupled with a low  $i_{\text{corr}}$  value are considered to have better corrosion resistance. Analysis of the corrosion data clearly identifies the more corrosion resistant alloy, and analysis of the surface and microstructure reveals that both alloy surfaces are not resistant to  $\text{Cl}^-$  ion attack.

### **4.3.1 Corrosion Analysis of AlCuNiMn**

#### ***4.3.1.1 Potentiodynamic Polarization Results***

Figure 24 includes the potentiodynamic polarization curves for the four AlCuNiMn alloy samples from the corrosion experiments carried out in a 3.5wt% NaCl solution. These four samples were in the as-received and annealed (600°C, 800°C, and 1000°C) conditions prior to corrosion testing. A summary of the corrosion data is summarized in Table 11 as a function annealing temperature. A comparison of the average  $E_{\text{corr}}$  value for the 1000°C annealed sample (-147.1 mV) compared to the average value for the as-received sample (-944.7 mV), shows the former to be 798 mV more positive compared to the latter. In addition, the corrosion current density ( $i_{\text{corr}}$ ) decreases when the samples are annealed at higher temperatures, with the lowest average  $i_{\text{corr}}$  value for the sample annealed at 1000°C,  $14.30 \mu\text{A}/\text{cm}^2$ , compared to an average  $76.62 \mu\text{A}/\text{cm}^2$  for the as-received sample. Thus, the corrosion rate decreases from an average 3.52 mmpy (millimeters per year) for the as-received AlCuNiMn sample to an average 0.41 mmpy for the 1000°C sample (Table 11).

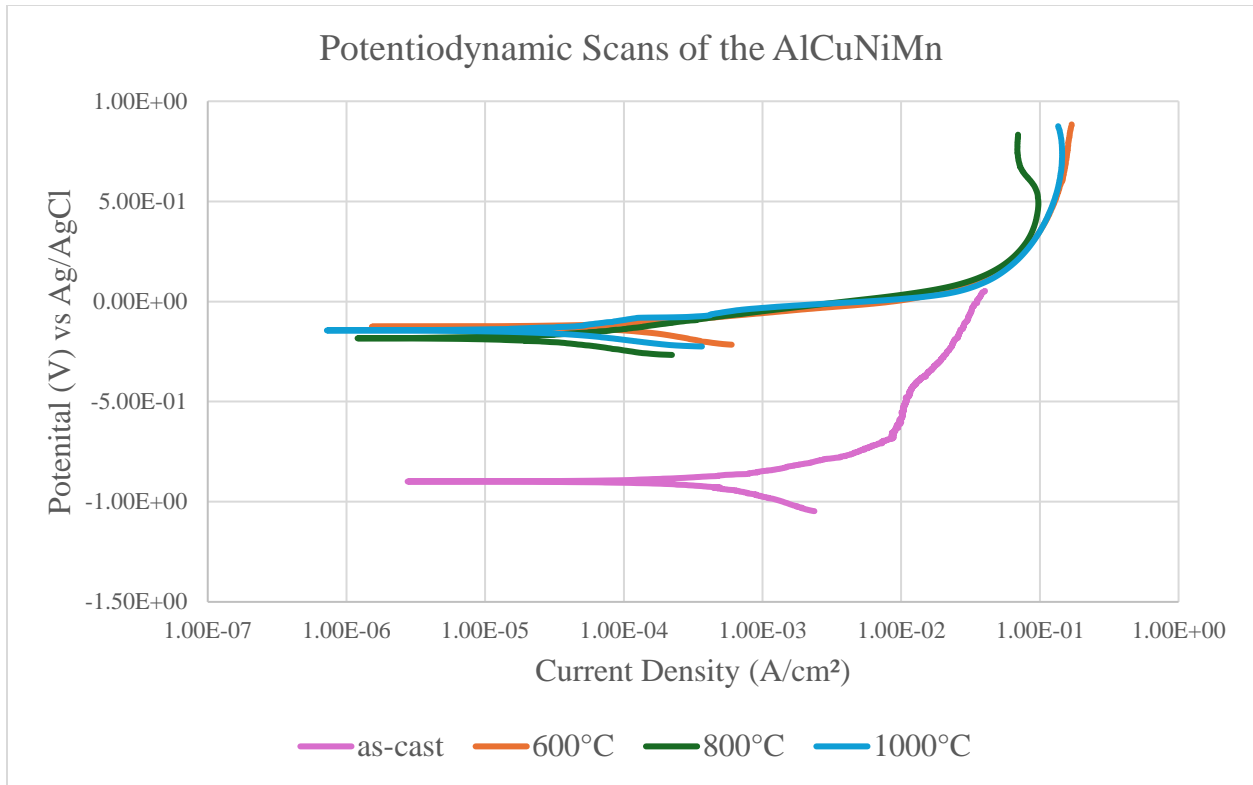


Figure 24. Potentiodynamic polarization curves of the as received and annealed (600°C, 800°C, and 1000°C) AlCuNiMn Alloy in 3.5wt% NaCl solution.

Table 11. Summary of corrosion data for as received and annealed (600°C, 800°C, and 1000°C) AlCuNiMn Alloy in 3.5wt% NaCl solution.

AlCuNiMn		$E_{corr}$ ( $mV_{Ag/AgCl}$ )	$i_{corr}$ ( $\mu A/cm^2$ )	Rp (kohms)	Corrosion rate (mmpy)
as received	Test 1	-962.2	99.92	0.2607	3.520
	Test 2	-927.1	53.32	0.4887	1.878
	<b>Average</b>	<b>-944.7</b>	<b>76.62</b>	<b>0.3747</b>	<b>2.699</b>
600°C	Test 1	-110.5	59.85	0.4353	2.108
	Test 2	-118.9	53.7	0.4851	1.892
	<b>Average</b>	<b>-114.7</b>	<b>56.78</b>	<b>0.4602</b>	<b>2.000</b>
800°C	Test 1	-130.3	21.53	1.21	0.758
	Test 2	-168.7	11.73	2.222	0.413
	<b>Average</b>	<b>-149.5</b>	<b>16.63</b>	<b>1.716</b>	<b>0.586</b>
1000°C	Test 1	-168.5	19.93	1.307	0.568
	Test 2	-125.7	8.671	3.005	0.247
	<b>Average</b>	<b>-147.1</b>	<b>14.30</b>	<b>2.156</b>	<b>0.408</b>

#### ***4.3.1.2 Microstructural Analysis of AlCuNiMn After Corrosion***

The corrosion rate of the AlCuNiMn alloy decreases as the annealing temperature is increased from 600°C to 1000°C. This may be due to the AlCuNiMn microstructure becoming more uniform as the annealing temperature of the sample is increased. Both the  $E_{\text{corr}}$  value and  $i_{\text{corr}}$  values are improving as the heat treatment temperature applied to AlCuNiMn is increased (prior to corrosion testing). Comparing the SEM Figures 8, 14, 15 and 16 (surfaces prior to corrosion) to Figures 25, 26, 28 and 30 (surfaces after corrosion), it is clear that the NaCl solution is interacting with the surface during corrosion testing. Examining the EDS mapping for each sample after corrosion, it is apparent that all the corroded AlCuNiMn surfaces are covered by an oxide formation that was not present after annealing and before the corrosion experiments. More details about relevant microstructural features for each sample are summarized below.

##### **As-received AlCuNiMn Sample**

In most corrosion studies of HEAs, the focus is on the as-received condition, which is prone to contain defects. In this study, voids are observed in the as-received condition for the AlCuNiMn alloy. However, applying an appropriate heat treatment is shown to promote a more uniform structure and elemental distribution, and this has been proven to improve the corrosion resistance as discussed previously in section 4.3.1.1. As the annealing temperature is increased, the microstructure of the alloy becomes more organized and well-behaved, including the size and depth of the voids (see Figure 17). Annealing at 1000°C decreases the compositional differences in the microconstituents and the uniformity of the microstructure is enhanced.

After the corrosion experiments, the use of SEM, EDS and XRD assisted with the identification of possible surface damage, oxide film formation, and corrosion products on the

surfaces of the AlCuNiMn alloy samples after exposure to the 3.5wt% NaCl solution. SEM examination of the as-received AlCuNiMn sample surface shows that the NaCl solution attacked the surface (Figure 25). EDS analysis reveals the presence of an oxide, and the oxygen EDS map aligns very well with the Al EDS map, with a slight overlap with Cu and Ni. However, XRD analysis did not detect an oxide on the surface. It is possible that the thickness of the oxide is relatively thin as it was not thick enough to be detected.

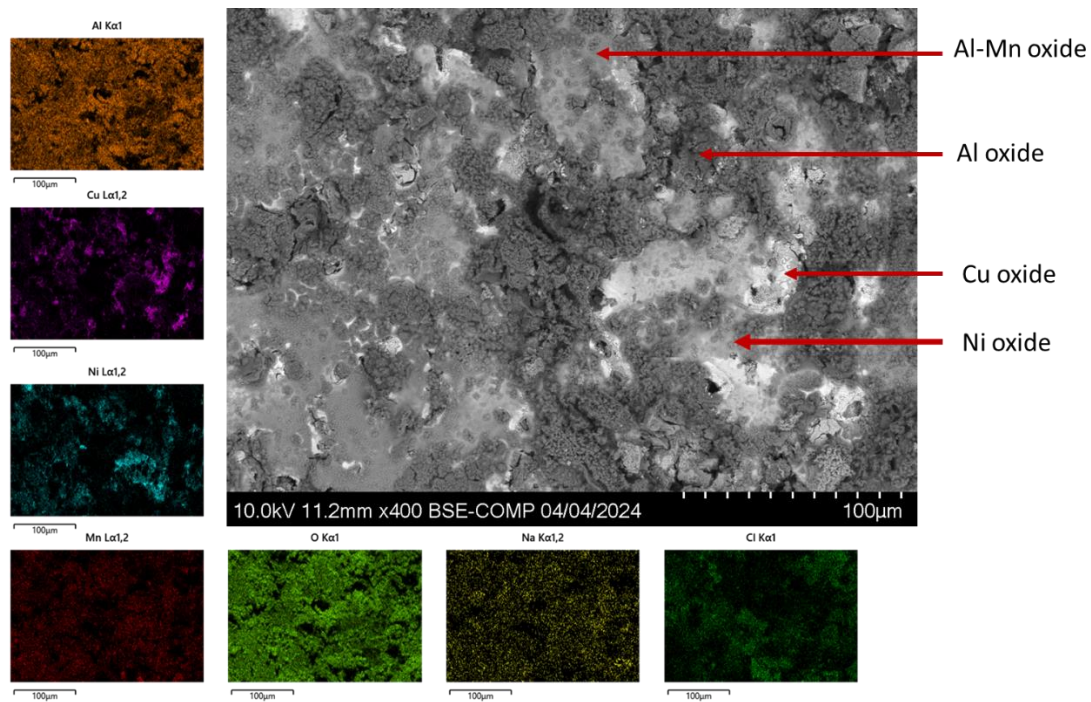


Figure 25. Microstructure of the as-received AlCuNiMn after immersion in 3.5 wt.% NaCl solution along with EDS analysis with individual element mapping.

#### AlCuNiMn Sample Annealed at 600°C

The corroded microstructure of the AlCuNiMn sample (annealed at 600°C prior to corrosion testing) is shown in the SEM image in Figure 26 with a corresponding XRD pattern in Figure 27. The original microstructure (Figure 14) is not visible due to corrosion, but AlCuNiMn-rich regions are still detected by EDS in between the corrosion product. XRD

analysis identified the existence of several corrosion products, including  $CuCl$  and  $CuCl_2$ . XRD also detected a Mn and Al oxide. The formation of a Mn oxide,  $Mn_2O_3$ , was also observed after annealing at  $600^\circ C$ .

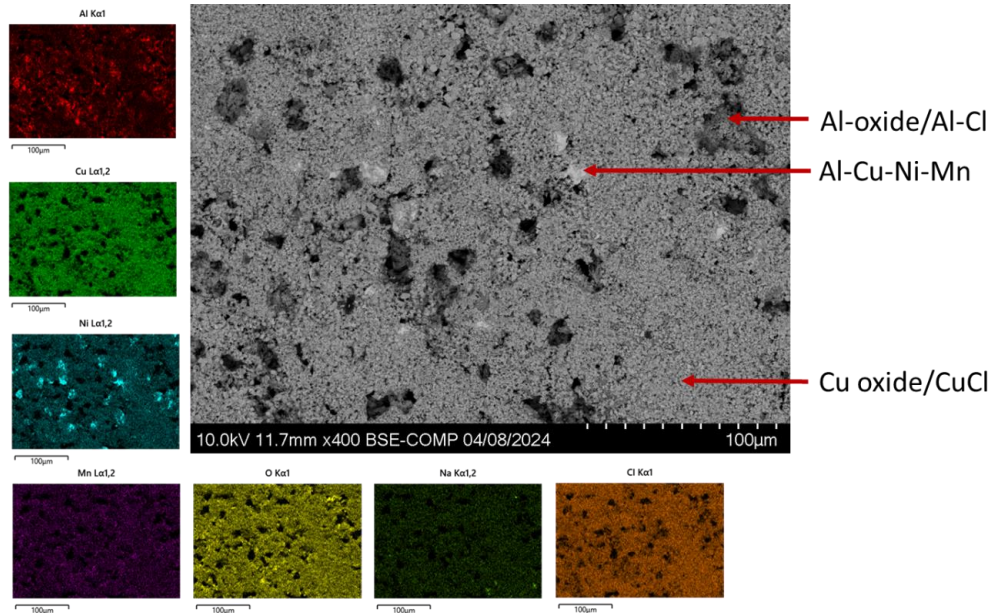


Figure 26. Microstructure of the AlCuNiMn annealed at  $600^\circ C$  Al-Cu-Ni-Mn after immersion in 3.5 wt.% NaCl solution along with EDS analysis with individual element mapping.

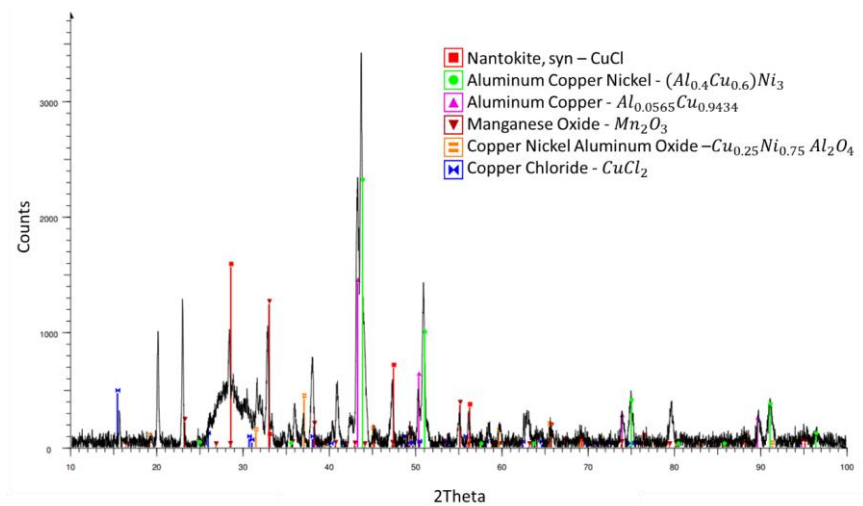


Figure 27. XRD pattern of the AlCuNiMn (annealed at  $600^\circ C$ ) after immersion in 3.5 wt.% NaCl solution.

## AlCuNiMn Sample Annealed at 800°C

The corroded microstructure of the AlCuNiMn sample (annealed at 800°C prior to corrosion testing) is shown in the SEM image in Figure 28 with a corresponding XRD pattern in Figure 29. As with the 600°C sample, the original microstructure (Figure 15) is not visible and the AlCuNiMn-rich regions are still detected by EDS in between the corrosion product. Pitting and/or pores are also visible within the oxide layer. XRD analysis revealed the presence of several corrosion products including *CuCl*. XRD also detected the same  $Mn_2O_3$  and  $CuMn_2O_4$  present after annealing at 800°C, in addition to other Mn oxides.

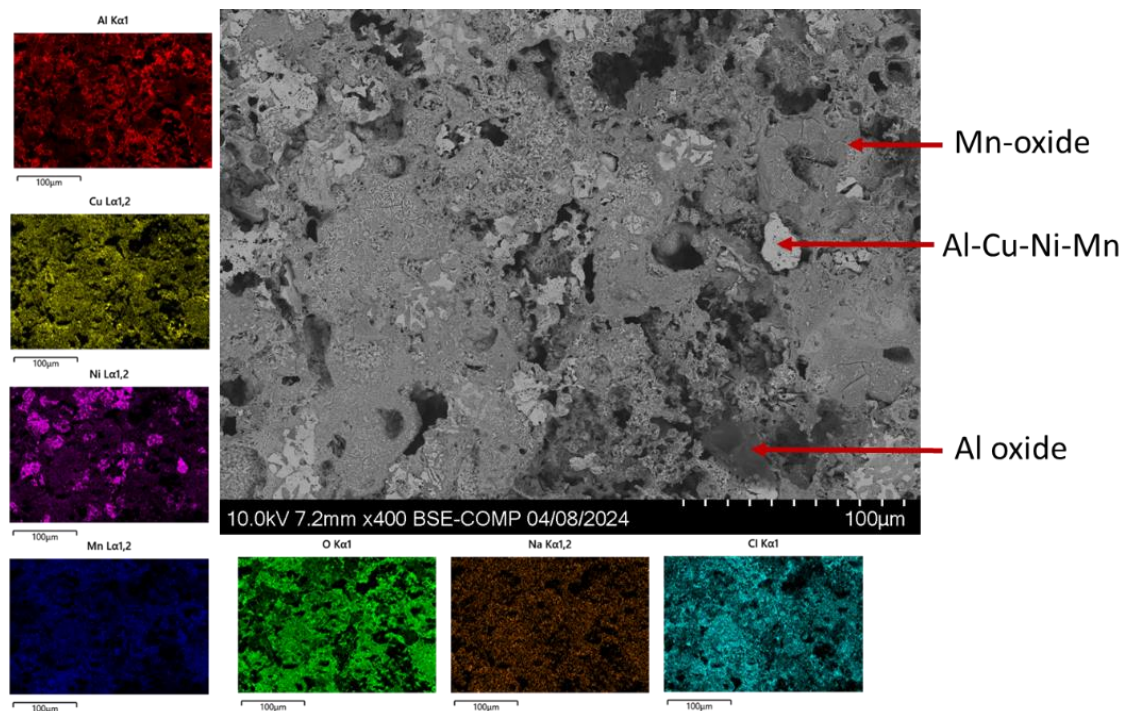


Figure 28. Microstructure of the AlCuNiMn (annealed at 800°C) after immersion in 3.5 wt.% NaCl solution along with EDS analysis with individual element mapping.

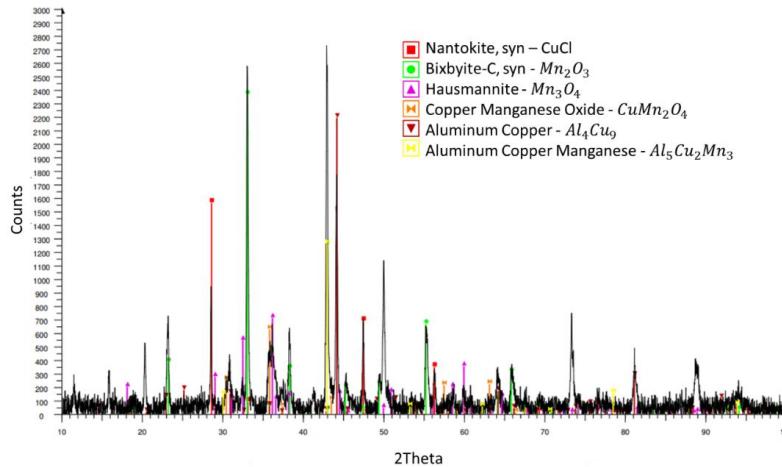


Figure 29. XRD pattern of the AlCuNiMn (annealed at 800°C) after immersion in 3.5 wt.% NaCl solution.

#### AlCuNiMn Sample Annealed at 1000°C

The corroded microstructure of the AlCuNiMn sample annealed at 1000°C is shown in the SEM image with elemental mapping in Figure 30, along with its corresponding XRD spectra in Figure 31. CuNiMn-rich areas are present before corrosion in the 1000°C surface and are also detected by EDS after corrosion. Pitting and/or pores are also visible within the oxide layer, but to a greater extent compared to the samples at 600°C and 800°C. XRD analysis revealed the presence of several corrosion products including *CuCl*. XRD also detected  $Al_2O_3$  and  $CuAlO_2$  present after annealing at 1000°C.

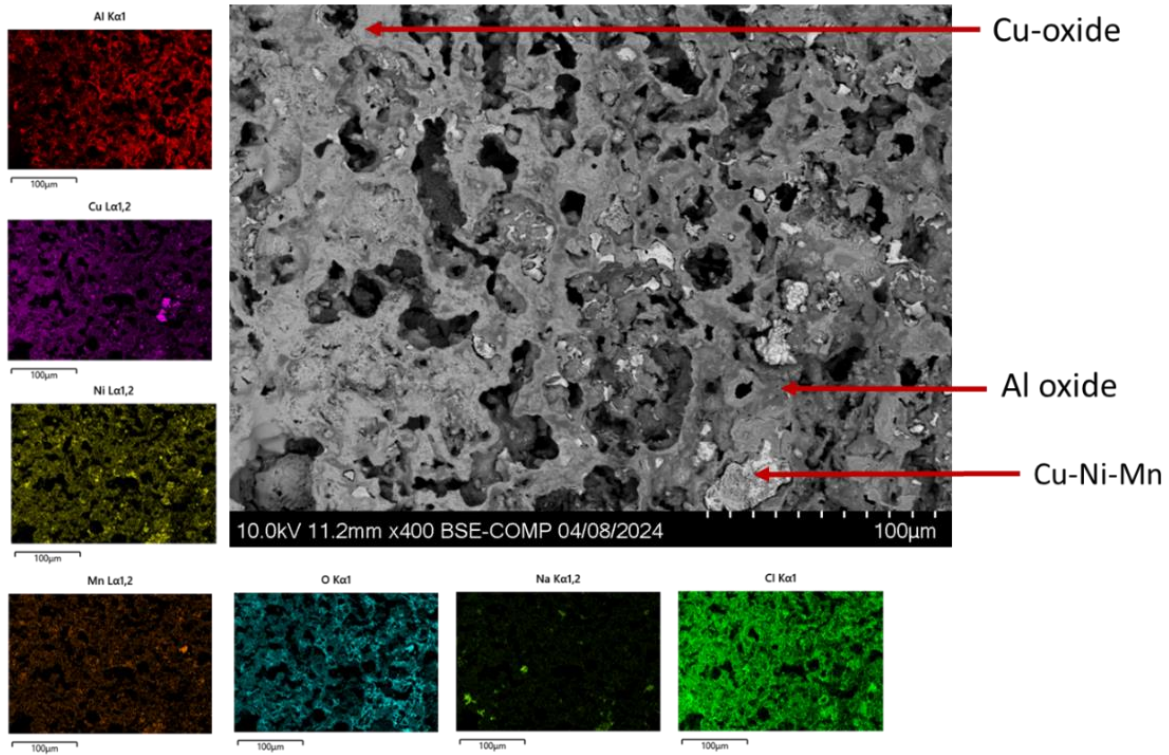


Figure 30. Microstructure of the AlCuNiMn (annealed at 1000°C prior to corrosion testing) after immersion in 3.5 wt.% NaCl solution along with EDS analysis with individual element mapping.

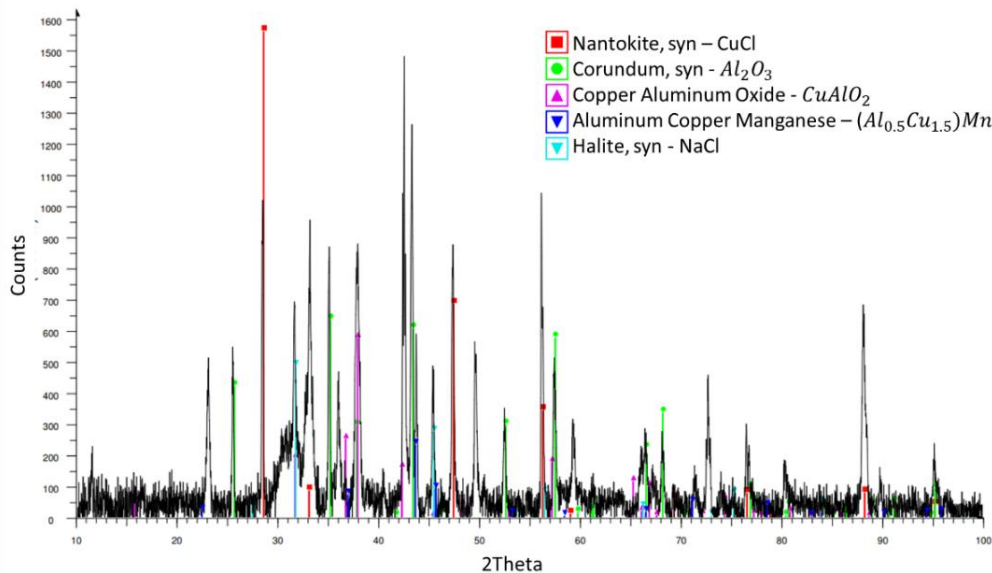


Figure 31. XRD pattern of the AlCuNiMn annealed at 1000°C Al-Cu-Ni-Mn after immersion in 3.5 wt.% NaCl solution.

## Summary of Corrosion of AlCuNiMn Sample

Table 12 summarizes the XRD data for corrosion products on the AlCuNiMn surfaces after corrosion testing with respect to the annealing temperature. The SEM images show surfaces that were electrochemically attacked and the formation of surface oxides. For samples annealed at 600°C and 800°C,  $Mn_2O_3$  is identified, which is also present after the annealing process.

Table 12. Summary of XRD data for corrosion products on each AlCuNiMn sample based on annealing temperature.

AlCuNiMn		
600°C	800°C	1000°C
CuCl	CuCl	CuCl
$Mn_2O_3$	$Mn_2O_3$	$Al_2O_3$
$Cu_{0.25}Ni_{0.75}Al_2O_4$	$Mn_3O_4$	$CuAlO_2$
$CuCl_2$	$CuMn_2O_4$	

### 4.3.2 Corrosion Analysis of AlCuNiMnSi

#### 4.3.2.1 Potentiodynamic Polarization Results for AlCuNiMnSi

The corrosion testing of three AlCuNiMnSi samples is discussed here, the as-received, and the samples annealed at 600°C and 800°C prior to corrosion testing. Figure 32 includes the polarization curves of the three AlCuNiMnSi alloy samples in 3.5 wt.% NaCl solution, and a summary of the corrosion data is listed in Table 13. There is no significant difference between the average  $E_{corr}$  values of the three AlCuNiMnSi samples. Their difference is within a range of only 32 mV. The average corrosion current density,  $i_{corr}$  increases slightly for the samples that experienced an annealing treatment prior to corrosion testing compared to the average value of the as-received sample. The lowest  $i_{corr}$  value,  $2.6 \mu A/cm^2$ , is observed for the as-received AlCuNiMnSi sample, with a corresponding corrosion rate of 0.08 mmpy (millimeters per year) and increases to  $12.1 \mu A/cm^2$  for the sample that was annealed at 800°C prior to corrosion testing, with a corresponding corrosion rate of 0.37 mmpy. This indicates that, although all the

average corrosion rates of the AlCuNiMnSi samples are all lower than those of the AlCuNiMn samples, the corrosion rates of the AlCuNiMn samples decrease with an increase in annealing temperature, while the average corrosion rates of the AlCuNiMnSi samples increase as the annealing temperature is increased.

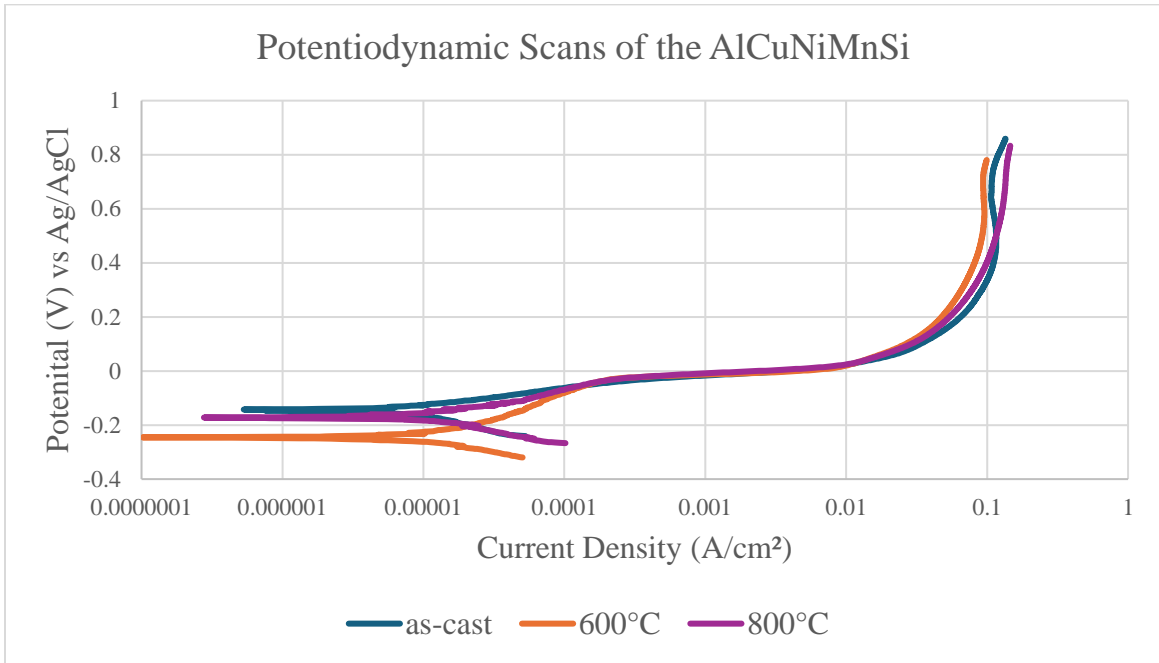


Figure 32. Potentiodynamic polarization curves of the as-received and annealed (600°C, 800°C, and 1000°C) AlCuNiMnSi Alloy in 3.5wt% NaCl solution.

Table 13. Summary of corrosion data for as received and annealed (600°C, 800°C, and 1000°C) AlCuNiMnSi Alloy in 3.5wt% NaCl solution.

AlCuNiMnSi		$E_{corr}$ ( $mV_{Ag/AgCl}$ )	$I_{corr}$ ( $\mu A/cm^2$ )	Rp (kohms)	Corrosion rate (mmpy)
as-received	Test 1	-157.8	2.546	10.23	0.079
	Test 2	-136.8	2.681	9.716	0.083
	<b>Average</b>	<b>-147.3</b>	<b>2.614</b>	<b>9.973</b>	<b>0.081</b>
600°C	Test 1	-111.9	5.265	4.949	0.163
	Test 2	-226.2	5.162	5.047	0.160
	<b>Average</b>	<b>-169.1</b>	<b>5.214</b>	<b>4.998</b>	<b>0.161</b>
800°C	Test 1	-114.9	16.15	1.613	0.499
	Test 2	-158.7	8.066	3.23	0.249
	<b>Average</b>	<b>-136.8</b>	<b>12.11</b>	<b>2.4215</b>	<b>0.374</b>

#### ***4.3.2.2 Microstructural Analysis of AlCuNiMnSi After Corrosion***

The corrosion rate of the AlCuNiMnSi alloy increases slightly as the annealing temperature increases from 600°C to 800°C. The values range from 0.08 mmpy (millimeters per year) for the as-received sample to 0.37 mmpy for the sample annealed at 800°C. The influence of annealing temperature results in a slight increase in the corrosion rate for the AlCuNiMnSi alloy, and the reverse is true for the AlCuNiMn alloy. However, the passivation curve for the AlCuNiMnSi samples (Figure 32) indicates that this sample is more effective at halting the current compared to any of the AlCuNiMn samples (Figure 24). There are two reasons as to why the AlCuNiMnSi alloy may be superior to the AlCuNiMn alloy. One is the presence of voids in the as-received AlCuNiMn samples, which are reduced while the microstructure becomes more uniform with an increase in annealing temperature. The second reason is the presence of the MnSi-rich microconstituent in the as-received AlCuNiMnSi alloy that is detected by EDS mapping before and after corrosion, as can be seen by comparing Figures 10 and 33, respectively, indicating that this region is resistant to corrosion. More details about relevant microstructural features for each sample are summarized below.

##### **As-received AlCuNiMnSi Sample**

The corroded surface of the AlCuNiMnSi alloy in the as-received condition is shown in Figures 33 and 34. The EDS mapping in Figure 33 is evidence of (1) CuCl surface contamination (due to reaction of Cu and Cl ions in solution on the sample surface), (2) the presence of Si and Al oxides, and (3) the intact MnSi-rich regions. Figure 34 is a comparison of BSE and SE surface SEM images and emphasizes the topographical features of the surface. XRD results of all three samples (as-received, 600°C and 800°C) are included in Figure 35. The XRD spectra confirms the presence of CuCl on all three surfaces and what appears to be the unaffected Mn-Si

rich microconstituent identified as  $Mn_5Si_3$ . The possible formation of an oxide or oxides (as detected by EDS) are not detected by XRD Analysis.

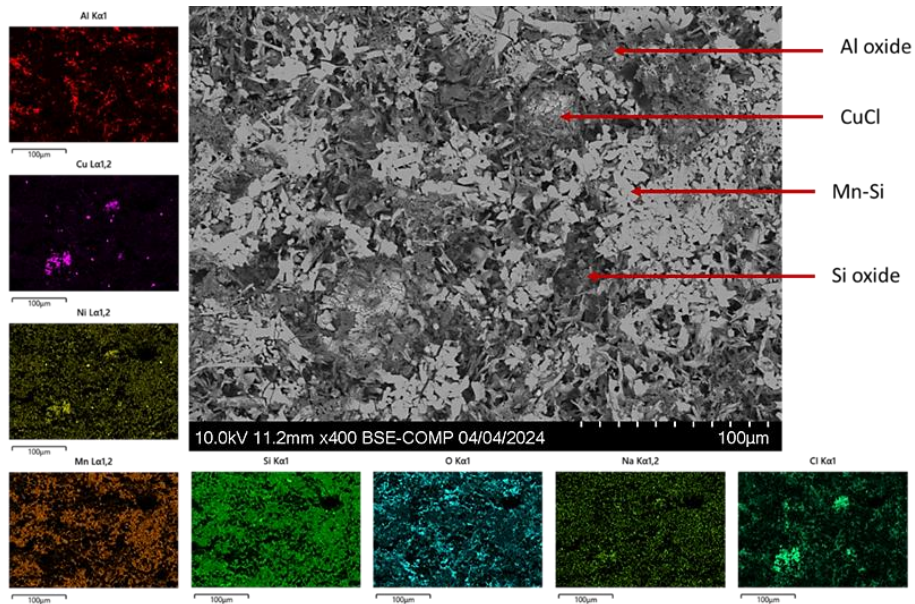


Figure 33. SEM BSE micrograph of the as-received AlCuNiMnSi after immersion in 3.5 wt.% NaCl solution along with EDS analysis with individual element mapping.

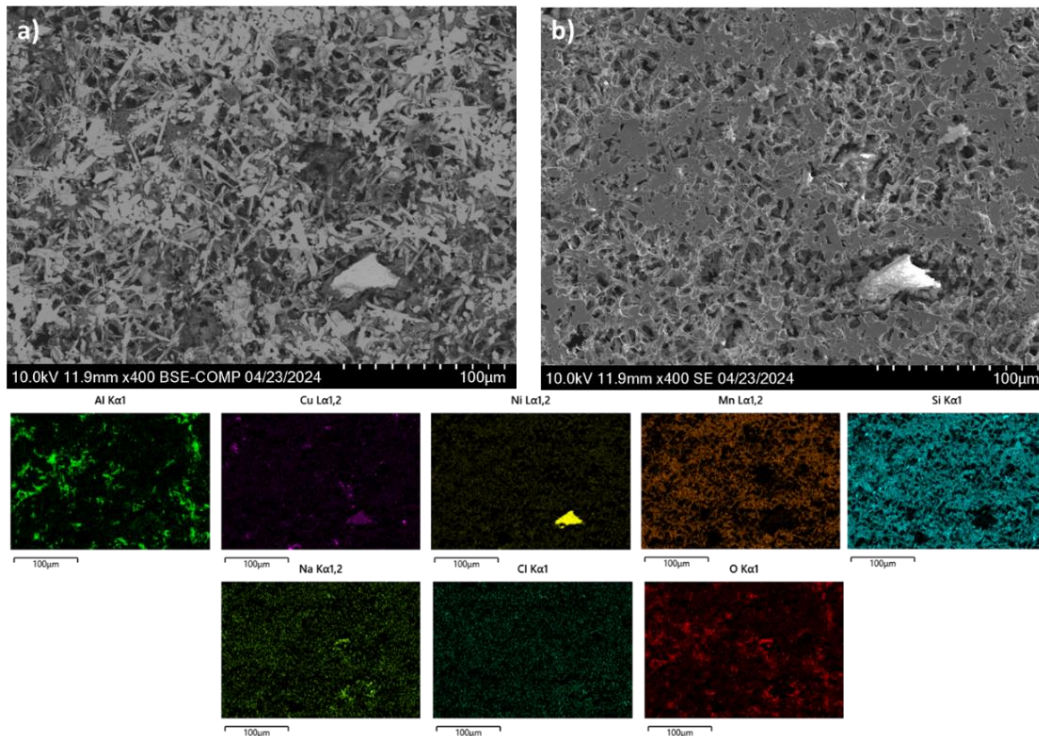


Figure 34. Microstructure of the corroded as-received AlCuNiMnSi with (a) BSE and (b) SE imaging with EDS scans of each individual element.

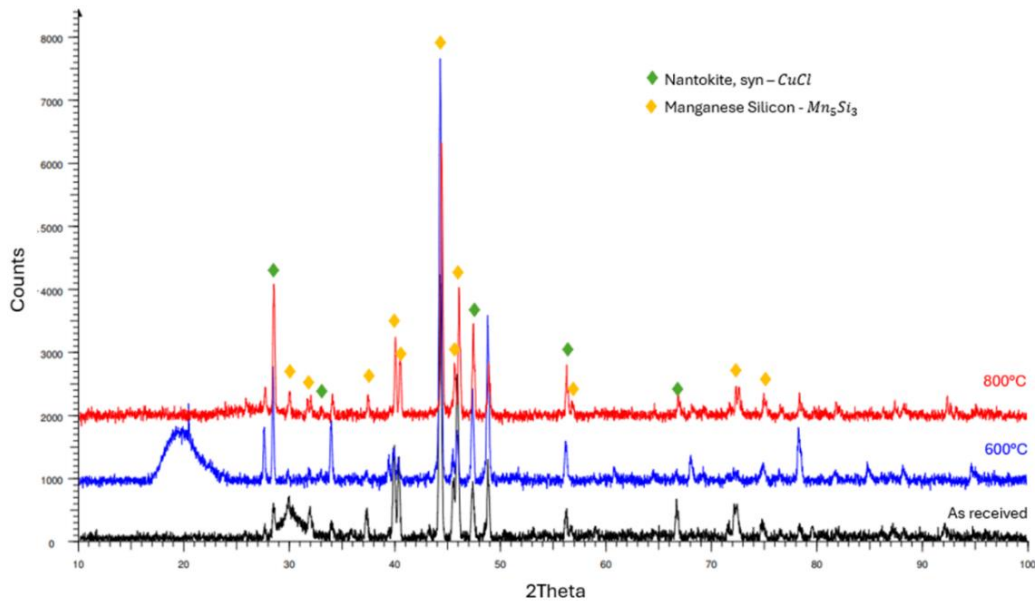


Figure 35. XRD patterns of the AlCuNiMnSi for the as-received sample, the annealed sample at 600°C, and the annealed sample at 800°C after immersion in 3.5 wt.% NaCl solution.

#### AlCuNiMnSi Sample Annealed at 600°C

Figure 36 includes an SEM image with EDS mapping of the corroded surface for the AlCuNiMnSi sample that was annealed at 600°C prior to corrosion testing. While the Ni- and MnSi-rich microconstituents are still visible, the AlCuNi-rich phase that was present after annealing and before corrosion testing, is not readily identifiable. This may be due to galvanic corrosion driven by the different potentials of the microconstituents, indicating that regions with high amounts of Al (such as AlCuNi-rich), are acting as the anodes that corrode, see figure 37. There is also evidence of oxide formation, since the Si and O align very well in the EDS mapping in Figure 36.

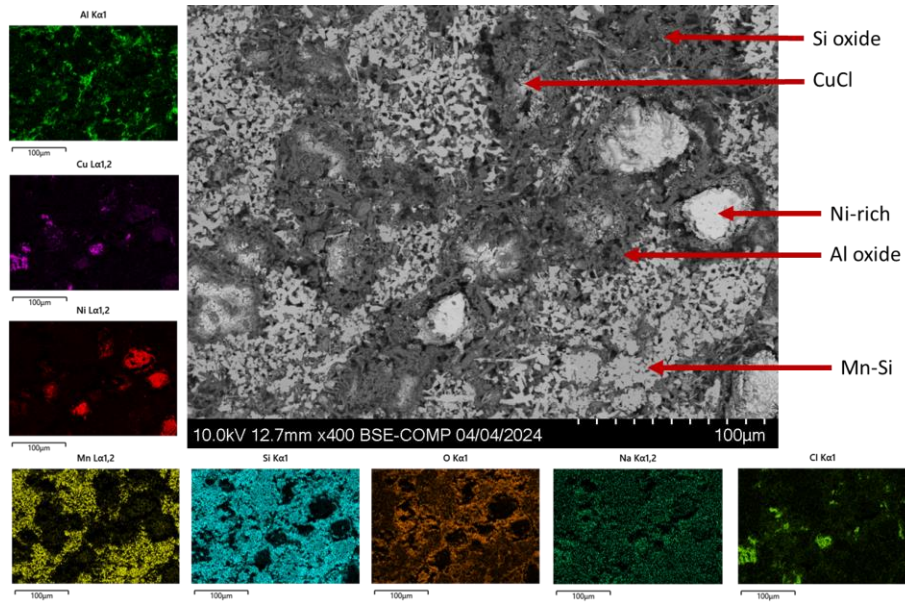


Figure 36. Microstructure of the AlCuNiMnSi annealed at 600°C after immersion in 3.5 wt.% NaCl solution along with EDS analysis with individual element mapping.

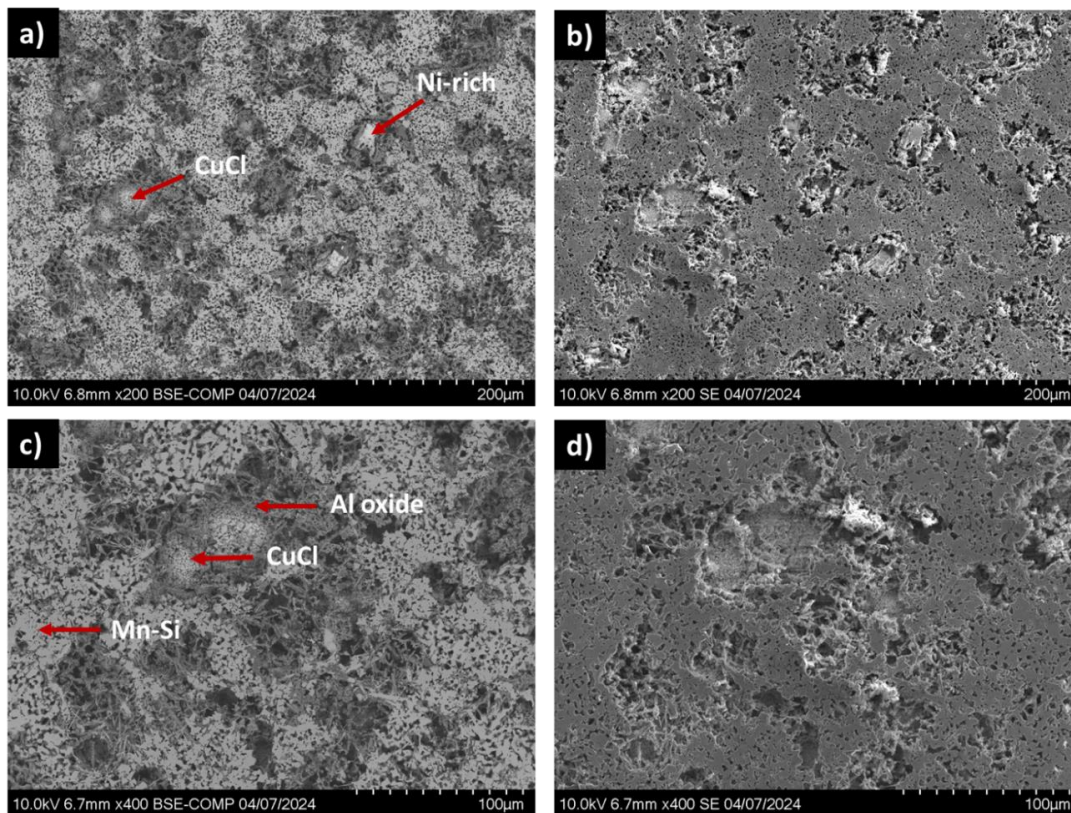


Figure 37. Corroded surface of the annealed (at 600° C) AlCuNiMnSi with (a) BSE and (b) SE imaging at 200x, and with (c) BSE and (d) SE imaging at 400x.

## AlCuNiMnSi Sample Annealed at 800°C

Annealing the AlCuNiMnSi sample at 800°C eliminates the presence of Ni in the microstructure but retains the AlCuNi- and MnSi-rich phases. After corrosion testing in NaCl, the MnSi-rich phase is still easily identifiable by EDS mapping in Figure 38. However, the Al signal is weak when compared to Cu and Ni, so the EDS signal for the AlCuNi-rich microconstituent is relatively low. As with the 600°C alloy, it is possible that the Al in the AlCuNi is being preferentially attacked.

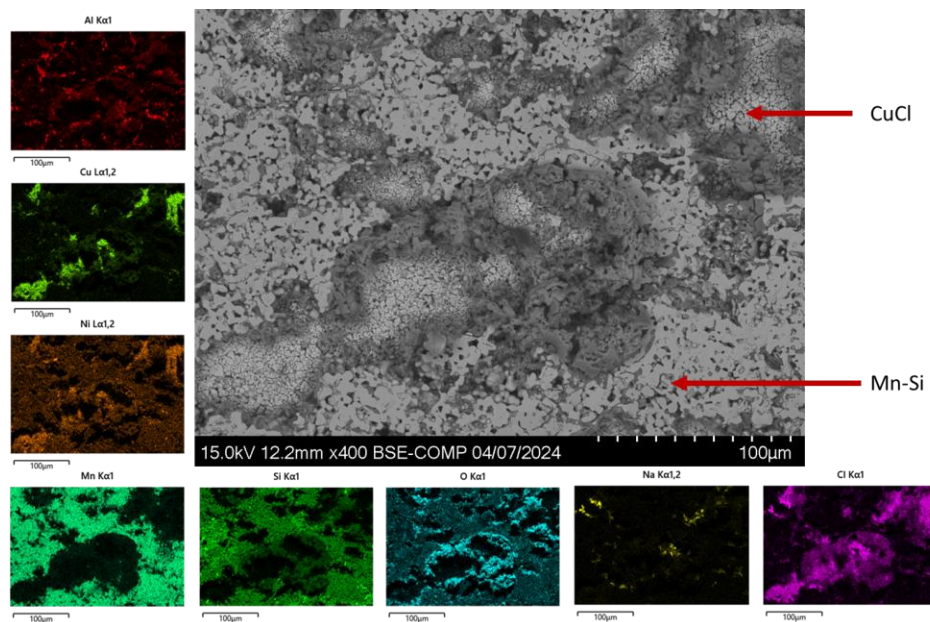


Figure 38. Microstructure of the AlCuNiMnSi annealed at 800°C after immersion in 3.5 wt.% NaCl solution along with EDS analysis with individual element mapping.

The corroded surface appearances of the as-received and annealed AlCuNiMnSi alloys are shown in Figure 39. The CuCl formation is increasing while the MnSi-rich region is decreasing with temperature. Due to increasing formations of CuCl throughout the microstructure, it makes sense as to why the corrosion rate is increasing. Although the corrosion

rate is increasing, it is not a drastic increase.

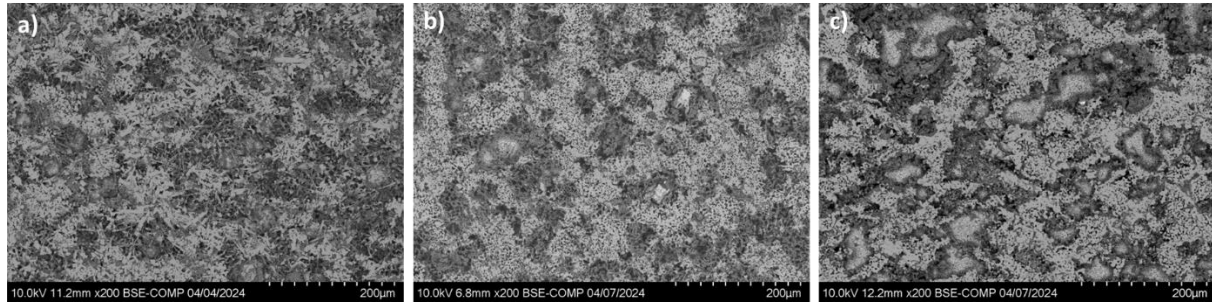


Figure 39. Corroded microstructures of the a) as received, b) annealed at 600°C, and c) annealed at 800°C Al-Cu-Ni-Mn-Si HEA from chloride-ion attack.

### 4.3.3 Comparison

In the as received conditions, Si addition does play a major role in the corrosion resistance. The addition of Si leads to the formation of a MnSi-rich constituent and a Ni-rich region with a trace of Si, both of which appear to be corrosion resistant. The as-received Si sample demonstrates the best corrosion resistance while the corrosion rate for the as-received AlCuNiMn alloy is the highest of all the samples tested. Figure 40 includes the potentiodynamic scans for the as-received AlCuNiMn and AlCuNiMnSi samples in 3.5wt% NaCl solutions (two trials each). It can be observed that the addition of Si to AlCuNiMn results in a clean transition from the anodic to the passive region, while the passivation for the base AlCuNiMn alloy indicates a weaker protection based on the smaller slope of the passive region.

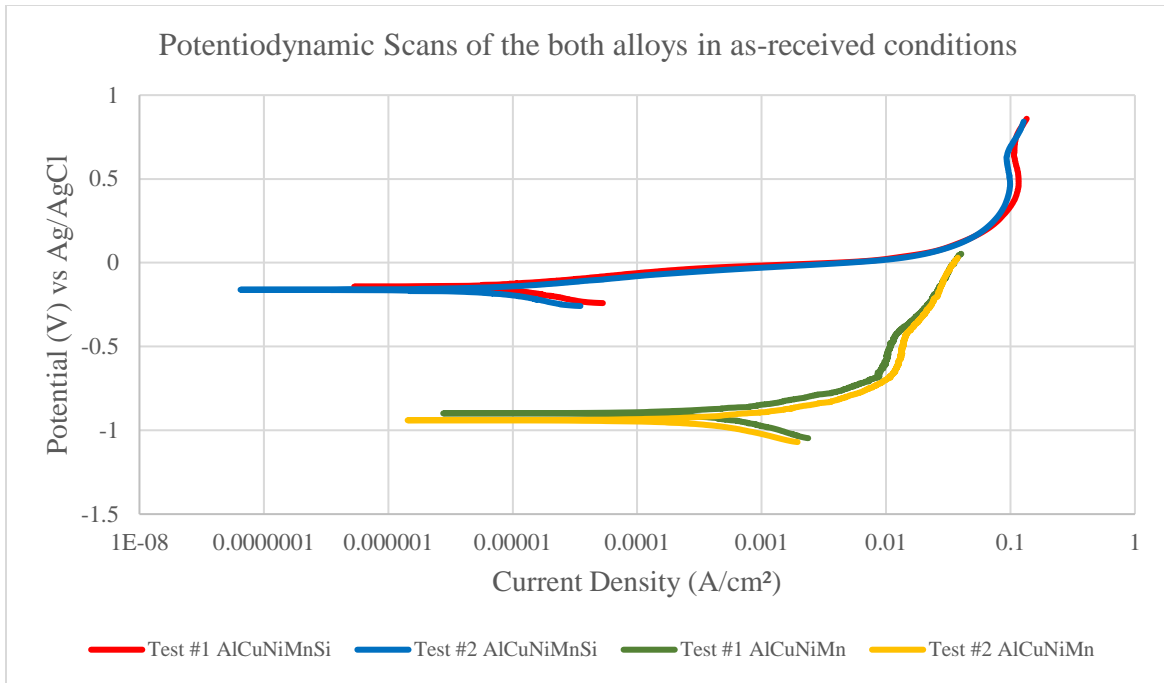


Figure 40. Comparison of potentiodynamic curves for both the AlCuNiMn and AlCuNiMnSi alloys in the as received condition immersed in 3.5wt% NaCl solution at room temperature.

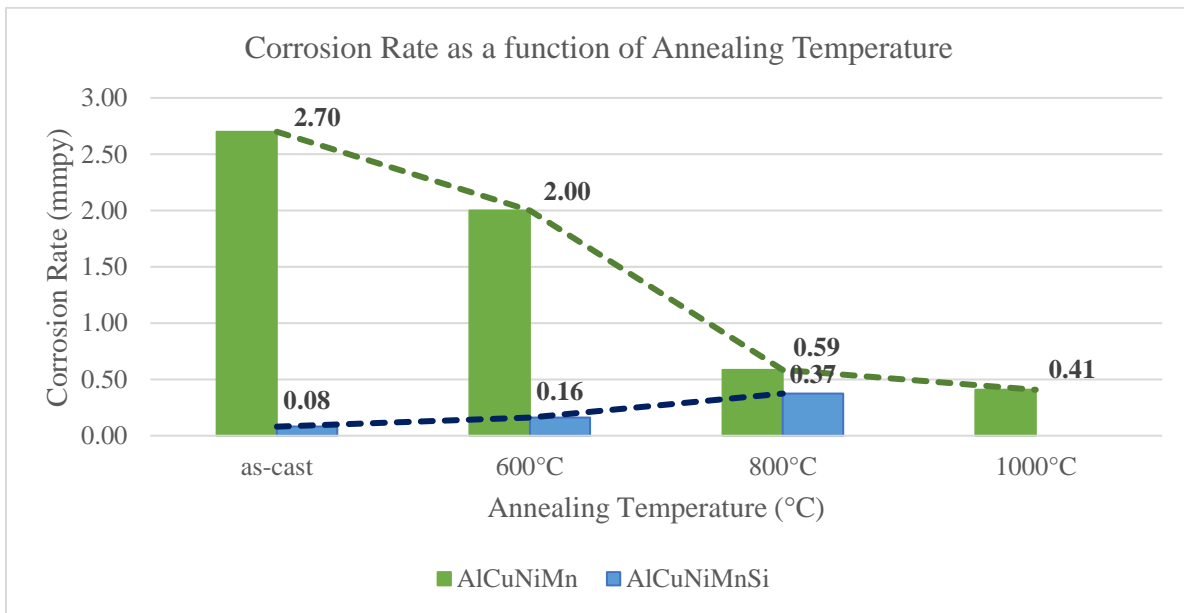


Figure 41. Corrosion rates of the AlCuNiMn and the AlCuNiMnSi alloys for samples in the as-received condition, and for samples annealed at various temperatures prior to corrosion testing.

## 5. Discussion

### 5.1 IMPACT OF THE MICROSTRUCTURE EVOLUTION ON THE CORROSION RESISTANCE OF ALCuNiMn

The addition of Al to another alloy system, the CoCrFeNi alloy, decreases the corrosion resistance due to the evolution of a second phase (AlNi-rich region) and relative increase to Al-oxide content, providing an unstable and weak protective film against chloride ion attack [5]. Shi et al. [53] applied a heat treatment at 1250°C for 1000 hours to homogenize the microstructure and reduce the elemental segregation, which decrease the phase fraction of the AlNi-rich region. Due to less formations of the Al-Ni rich phase, it improved the corrosion resistance of the alloy. Another similar outcome, aging the CoCrFeNiCu HEA at 1250C for 24 hours reduces the corrosion rate as it successfully dissolves the Cu-rich phase into the CoCrFeNi rich matrix [42].

In this study, a similar outcome is analyzed as in the as-received condition resulted in the worst corrosion properties compared to the other alloys investigated in this paper. Applying an appropriate heat treatment is essential for microstructure morphology, elemental distribution, and properties of the alloy. Figure 42 illustrates how the microstructure of the ALCuNiMn alloy is modified due to the annealing treatment. A more homogenized microstructure is created and the compositional differences between the constituents is minimized and in turn improving the corrosion resistance of the alloy.

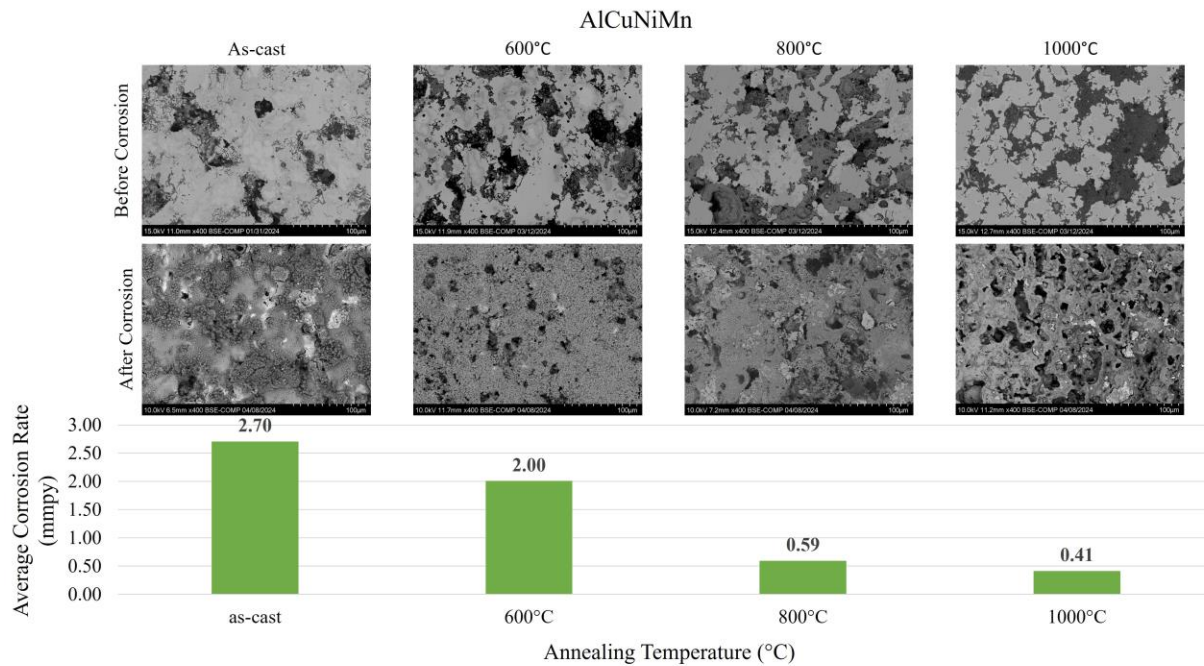


Figure 42. Corrosion rate of AlCuNiMn as a function of annealing temperature with illustrations of sample surfaces before and after corrosion testing.

## 5.2 IMPACT OF THE MICROSTRUCTURE EVOLUTION ON THE CORROSION RESISTANCE OF ALCuNiMnSi

Introducing Si to the AlCuNiMn alloy system improves the corrosion resistance. However, the corrosion resistance of this alloy decreases as a result of the pre-corrosion annealing treatments. Figure 43 illustrates the before and after corrosion microstructures and the corresponding corrosion rates. The Ni constituent has been identified as one of the factors contributing to the performance of the alloy's corrosion resistance. As the enrichment of those Ni areas decreases it results in a higher proportional area of the Al-rich containing regions. The already identified AlCuNi-rich region is known to be sensitive to corrosion as this has been reported from prior CoCrFeNiAl HEA studies. Since there are high contents of Al and Ni within the AlCuNi-rich constituent, it is believed to dissolve into the solution and redeposit as CuCl.

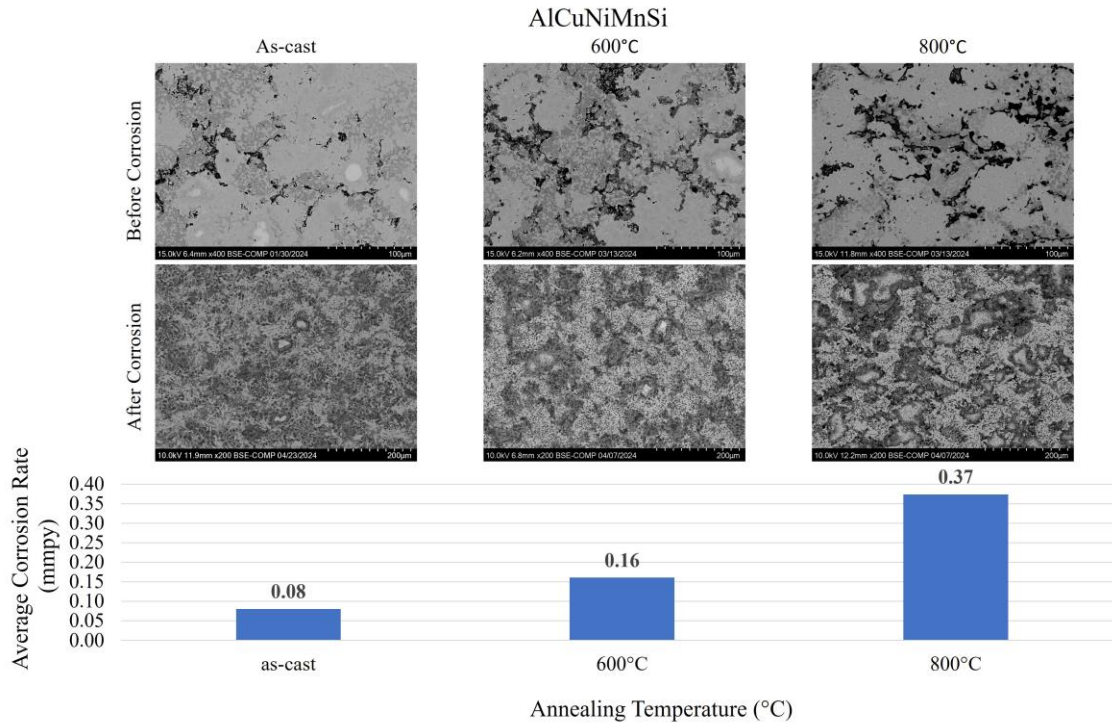


Figure 43. Corrosion rate of AlCuNiMnSi as a function of annealing temperature with illustrations of sample surfaces before and after corrosion testing.

Another studied HEA showing a similar outcome that the addition of the fifth alloying element may improve the corrosion resistance, subjecting heat treatment does not necessarily mean further improvement. As heat treatment can also negatively affect the corrosion resistance of the alloy. In the background section (Section 2.2.5), it was previously discussed on the effect of Mo on the CoCrFeNi-base alloy. Wang et al. [35] reports the effect of Mo on the CoCrFeNi-alloy system resulted in a new single phase solid solution and a wide passive region indicating a uniform, nonporous, and stable passive layer on the surface. The pitting resistance not only surpasses the 304 and 316L stainless steels but the CoCrFeNi alloy. Niu et al. [54] investigates the corrosion behavior of the as annealed CoCrFeNiMo HEAs. The Mo addition HEA is annealed at 900°C for 1 hour, it was determined that annealing induces instability and phase separation. Both literatures conducted their corrosion experiments in 3.5wt% NaCl solutions at room temperature. Table 14

provides the electrochemical corrosion properties of the as cast and as annealed of CoCrFeNiMo. Annealing the HEA results in a lower corrosion potential value and higher corrosion current density which expresses that annealing treatment decreases the corrosion resistance of the HEA.

Table 14. Electrochemical corrosion properties of the as cast and annealed CoCrFeNiMo in 3.5wt%NaCl solution at room temperature [35, 54].

Alloy System	$E_{corr}$ (V)	$i_{corr}$ (A/cm <sup>2</sup> )	References
As cast CoCrFeNi	-0.265	$3.17 \times 10^{-7}$	[35]
As cast CoCrFeNiMo <sub>0.2</sub>	-0.192	$1.84 \times 10^{-9}$	[35]
As annealed CoCrFeNi	-1.048	$6.445 \times 10^{-6}$	[54]
As annealed CoCrFeNiMo <sub>0.2</sub>	-1.047	$6.371 \times 10^{-6}$	[54]

## 6. Conclusions

- Microstructural changes are observed in both alloys as a result of increasing annealing temperatures, indicating that temperature has a major influence on the microstructure evolution for these specific alloy systems.
- Annealing of the AlCuNiMn alloy up to 1000°C prior to corrosion testing significantly enhances the microstructure uniformity and reduces the corrosion rate. This is proof that heat treatments can enhance the overall performance of HEAs.
- The as-received AlCuNiMnSi alloy demonstrated the best corrosion resistance in this study.
- The corrosion rates for the AlCuNiMnSi alloy increase with annealing temperature, however, all of the AlCuNiMnSi alloy samples outperformed the AlCuNiMn alloy samples.
- The MnSi-rich constituent in the AlCuNiMnSi alloy may be responsible for the corrosion resistance of the AlCuNiMnSi alloy.

## References

- [1] J.-W. Yeh, S.-K. Chen, S.-J. Lin, J.-Y. Gan, T.-S. Chin, T.-T. Shun, C.-H. Tsau and S.-Y. Chang, "Nanostructured High-Entropy Alloys with Multiple Principal Elements: Novel Alloy Design Concepts and Outcomes," *Advanced Engineering Materials*, vol. 6, no. 5, pp. 299-303, 2004.
- [2] C.-Y. Cheng, Y.-C. Yang, Y.-Z. Zhong, Y.-Y. Chen, T. Hsu and J.-W. Yeh, "Physical metallurgy of concentrated solid solutions from low-entropy to high-entropy alloys," *Current Opinion in Solid State and Materials Science*, vol. 21, no. 6, pp. 299-311, 2017.
- [3] W. Li, D. Xie, D. Li, Y. Zhang, Y. Gao and P. K. Liaw, "Mechanical behavior of high-entropy alloys," *Progress in Materials Science*, vol. 118, pp. 1-142, 2021.
- [4] D. B. Miracle and O. N. Senkov, "A critical review of high entropy alloys and related concepts," *Acta Materialia*, vol. 122, pp. 448-511, 2017.
- [5] Y. Fu, J. Li, H. Luo, C. Du and X. Li, "Recent advances on environmental corrosion behavior and mechanism of high-entropy alloys," *Journal of Materials Science and Technology*, vol. 80, pp. 217-233, 2021.
- [6] Y. Zhang, T. T. Zuo, Z. Tang, M. C. Gao, K. A. Dahmen, P. K. Liaw and Z. P. Lu, "Microstructures and properties of high-entropy alloys," *Progress in Materials Science*, vol. 61, pp. 1-93, 2014.
- [7] Z. Tang, L. Huang, W. He and P. K. Liaw, "Alloying and Processing Effects on the Aqueous Corrosion Behavior of High-Entropy Alloys," *Entropy*, vol. 16, pp. 895-911, 2014.
- [8] Y. Shi, B. Yang and P. K. Liaw, "Corrosion-Resistant High Entropy Alloys: A Review," *Metals*, vol. 7, no. 2, p. 43, 2017.
- [9] P. Muangtong, A. Rodchanarowan, D. Chaysuwan, N. Chanlek and R. Goodall, "The corrosion behavior of CoCrFeNi-x (x = Cu, Al, Sn) high entropy alloy systems in chloride solution," *Corrosion Science*, vol. 172, 2020.
- [10] Z. H. Jin, H. H. Ge, W. W. Lin, Y. W. Zong, S. J. Liu and J. M. Shi, "Corrosion behavior of 316L stainless steel and anti-corrosion materials in a high acidified chloride solution," *Applied Surface Science*, vol. 322, pp. 47-56, 2014.
- [11] G. S. Frankel, "Introduction to Metallurgically Influenced Corrosion," in *ASM Handbook Volume 13A: Corrosion Fundamentals, Testing, and Protection*, ASM International: Novely, OH, USA, 2003, p. 257.
- [12] H. Diao, L. J. Santodonato, Z. Tang, T. Egami and P. K. Liaw, "Local Structures of High-Entropy Alloys (HEAs) on Atomic Scales: An Overview," *JOM*, vol. 67, pp. 2321-2325, 2015.
- [13] Y.-J. Hsu, W.-C. Chiang and J.-K. Wu, "Corrosion behavior of FeCoNiCrCux high-entropy alloys in 3.5% sodium chloride solution," *Materials Chemistry and Physics*, vol. 92, no. 1, pp. 112-117, 2005.
- [14] Y.-F. Kao, T.-D. Lee, S.-K. Chen and Y.-S. Chang, "Electrochemical passive properties of Al<sub>x</sub>CoCrFeNi (x=0, 0.25, 0.5, 1.0) alloys in sulfuric acids," *Corrosion Science*, vol. 52, no. 3, pp. 1026-1034, 2010.

- [15] Y. Shi, B. Yang, X. Xie, J. Brechtel, K. A. Dahmen and P. K. Liaw, "Corrosion of Al<sub>x</sub>CoCrFeNi high-entropy alloys: Al-content and potential scan-rate dependent pitting behavior," *Corrosion Science*, vol. 119, pp. 33-45, 2017.
- [16] B. Cantor, I. T. H. Chang, P. Knight and A. J. B. Vincent, "Microstructural development in equiatomic multicomponent alloys," *Materials Science and Engineering: A*, Vols. 375-377, pp. 213-218, 2004.
- [17] C. Zhang, M. Zhu, Y. Yuan and S. Guo, "The effect of Mn addition on corrosion behaviour of equiatomic CoCrFeNi high entropy alloys in NaCl solution," *Corrosion Engineering, Science and Technology*, vol. 58, no. 2, pp. 169-179, 2023.
- [18] Z. Niu, J. Xu, T. Wang, N. Wang, Z. Han and Y. Wang, "Microstructure, mechanical properties and corrosion resistance of CoCrFeNiW<sub>x</sub> (x = 0, 0.2, 0.5) high entropy alloys," *Intermetallics*, vol. 112, 2019.
- [19] V. Firouzidor, K. Sridharan, G. Cao, M. Anderson and T. R. Allen, "Corrosion of a stainless steel and nickel-based alloys in high temperature supercritical carbon dioxide environment," *Corrosion Science*, vol. 69, pp. 281-291, 2013.
- [20] G. Victor, V. Lonelia, C. M. Cosmin, V. M. Diana, V. I. Mihai and M. R. J. Claudia, "Effect of Al on Corrosion Behavior in 3.5% NaCl Solution of Al<sub>x</sub>CoCrFeNi High Entropy Alloys," *International Journal of Engineering Research in Africa*, vol. 53, pp. 20-30, 2021.
- [21] W.-R. Wang, W.-L. Wang, S.-C. Wang, Y.-C. Tsai, C.-H. Lai and J.-W. Yeh, "Effects of Al addition on the microstructure and mechanical property of Al<sub>x</sub>CoCrFeNi high-entropy alloys," *Intermetallics*, vol. 26, pp. 44-51, 2012.
- [22] J. Y. He, W. H. Liu, H. Wang, Y. Wu, X. J. Liu, T. G. Nieh and Z. P. Lu, "Effects of Al addition on structural evolution and tensile properties of the FeCoNiCrMn high-entropy alloy system," *Acta Materialia*, vol. 62, pp. 105-113, 2014.
- [23] M. S. Parvizi, A. Aladjem and J. E. Castle, "Behaviour of 90-10 cupronickel in sea water," *International Materials Reviews*, vol. 33, no. 1, pp. 169-200, 1988.
- [24] W. Schleich, "Application of Copper-Nickel Alloy UNS C70600 for Seawater Service," *CORROSION*, 2005.
- [25] Z. G. Zhu, K. H. Ma and C. H. Shek, "Compositional dependence of phase formation and mechanical properties in three CoCrFeNi-(Mn/Al/Cu) high entropy alloys," *Intermetallics*, vol. 79, pp. 1-11, 2016.
- [26] S. B. Lyon, "3.12 - Corrosion of Tin and its Alloy," *Shreir's Corrosion*, vol. 3, pp. 2068-2077, 2010.
- [27] Z. Y. Zheng, X. C. Li, C. Zhang and J. C. Li, "Microstructure and corrosion behaviour of FeCoNiCuSn<sub>x</sub> high entropy alloys," *Materials Science and Technology*, vol. 31, no. 10, pp. 1148-1152, 2015.
- [28] I. D. Ryck, E. V. Biezen, K. Leyssens, A. Adriaens, P. Storme and F. Adams, "Study of tin corrosion: the influence of alloying elements," *Journal of Cultural Heritage*, vol. 5, pp. 189-195, 2004.
- [29] G. Bracq, M. Laurent-Brocq, L. Perriere, R. Pires, J.-M. Joubert and I. Guillot, "The fcc solid solution stability in the Co-Cr-Fe-Mn-Ni multi-component system," *Acta Materialia*, vol. 128, pp. 327-336, 2017.

- [30] C. Niu, C. R. LaRosa, J. Miao, M. J. Mills and M. Ghazisaeidi, "Magnetically-driven phase transformation strengthening in high entropy alloys," *Natural Communications*, vol. 9, p. 1363, 2018.
- [31] W. Kai, C. C. Li, F. P. Cheng, K. P. Chu, R. T. Huang, L. W. Tsay and J. J. Kai, "The oxidation behavior of an equimolar FeCoNiCrMn high-entropy alloy at 950C in various oxygen-containing atmospheres," *Corrosion Science*, vol. 108, pp. 209-214, 2016.
- [32] M. Zhu, B. Zhao, Y. Yuan, S. Yin, S. Guo and G. Wei, "Effect of annealing temperature on microstructure and corrosion behavior of CoCrFeMnNi high-entropy alloy in alkaline soil simulation solution," *Materials Chemistry and Physics*, vol. 279, p. 125725, 2022.
- [33] Z. Xu, H. Zhang, X. Du, Y. He, H. Luo, G. Song, L. Mao, T. Zhou and L. Wang, "Corrosion resistance enhancement of CoCrFeMnNi high-entropy alloy fabricated by additive manufacturing," *Corrosion Science*, vol. 177, 2020.
- [34] H. Luo, Z. Li, A. M. Mingers and D. Raabe, "Corrosion behavior of an equiatomic CoCrFeMnNi high-entropy alloy compared with 304 stainless steel in sulfuric acid solution," *Corrosion Science*, vol. 134, pp. 131-139, 2018.
- [35] Q. Wang, A. Amar, C. Jiang, H. Luan, S. Zhao, H. Zhang, G. Le, X. Liu, X. Wang, X. Yang and J. Li, "CoCrFeNiMo<sub>0.2</sub> high entropy alloy by laser melting deposition: Prospective material for low temperature and corrosion resistant applications," *Intermetallics*, vol. 119, 2020.
- [36] C. Dai, T. Zhao, C. Du, Z. Liu and D. Zhang, "Effect of molybdenum content on the microstructure and corrosion behavior of FeCoCrNiMox high-entropy alloys," *Journal of Materials Science & Technology*, vol. 46, pp. 64-73, 2020.
- [37] A. Raza, S. Abdulahad, B. Kang, H. J. Ryu and S. H. Hong, "Corrosion resistance of weight reduced AlxCrFeMoV high entropy alloys," *Applied Surface Science*, vol. 485, pp. 368-374, 2019.
- [38] C. S. Raju, D. Venugopal, P. R. Srikanth, K. Lokeshwaran, M. Srinivas, C. J. Chary and A. A. Kumar, "Effects of aluminum addition on the properties of CoCuFeNiTi high entropy alloys," *Materials Today: Proceedings*, vol. 5, no. 13, pp. 26823-26828, 2018.
- [39] B. Ren, Z. X. Liu, D. M. Li, L. Shi, B. Cai and M. X. Wang, "Corrosion behavior of CuCrFeNiMn high entropy alloy system in 1 M sulfuric acid solution," *Materials and Corrosion*, vol. 63, no. 9, pp. 828-834, 2011.
- [40] W. H. Wang, Z. G. Zheng, B. Huang, J. W. Lai, Q. Zhou, L. Lei and D. C. Zheng, "Magnetocaloric effect, corrosion and mechanical properties of Mn<sub>1.05</sub>Fe<sub>0.9P0.5</sub>Si<sub>0.5</sub>Cu<sub>x</sub> alloys," *Intermetallics*, vol. 113, 2019.
- [41] E. Zhou, D. Qiao, Y. Yang, D. Xu, Y. Lu, J. Wang, J. A. Smith, H. Li, H. Zhao, P. K. Liaw and F. Wang, "A novel Cu-bearing high-entropy alloy with significant antibacterial behavior against corrosive marine biofilms," *Journal of Materials Science and Technology*, vol. 46, pp. 201-210, 2020.
- [42] C.-M. Lin, H.-L. Tsai and H.-Y. Bor, "Effect of aging treatment on microstructure and properties of high-entropy Cu<sub>0.5</sub>CoCrFeNi alloy," *Intermetallics*, vol. 18, pp. 1244-1250, 2010.

- [43] X. Zhang, J. Guo, X. Zhang, Y. Song, Z. Li, X. Xing and D. Kong, "Influence of remelting and annealing treatment on corrosion resistance of AlFeNiCoCuCr high entropy alloy in 3.5% NaCl solution," *Journal of Alloys and Compounds*, vol. 775, pp. 565-570, 2019.
- [44] K. Masemola, P. Popoola and N. Malatji, "The effect of annealing temperature on the microstructure, mechanical and electrochemical properties of arc-melted AlCrFeMnNi equi-atomic high entropy alloy," *Journal of Materials Research and Technology*, vol. 9, no. 3, pp. 5241-5251, 2020.
- [45] L. L. Snead, D. T. Hoelzer, M. Rieth and A. A. Nemith, "Chapter 13 - Refractory Alloys: Vanadium, Niobium, Molybdenum, Tungsten,," in *Structural Alloys for Nuclear Energy Applications*, Elsevier, 2019, pp. 585-640.
- [46] F. Liu, P. K. Liaw and Y. Zhang, "Recent Progress with BCC-Structured High-Entropy Alloys," *Metals*, vol. 12, no. 3, p. 501, 2022.
- [47] S. K. Varma, F. Sanchez and C. V. Ramana, "Microstructures in a Nb-Cr-V-W-Ta high entropy alloy during annealing," *Journal of Materials Science and Technology*, vol. 53, pp. 66-72, 2020.
- [48] S. K. Varma, F. Sanchez, S. Moncayo and C. V. Ramana, "Static and cyclic oxidation of Nb-Cr-V-W-Ta high entropy alloy in air from 600 to 1400C," *Journal of Materials Science and Technology*, vol. 38, pp. 189-196, 2020.
- [49] B. Gorr, F. Mueller, H. J. Christ, T. Mueller, A. Kauffmann and M. Heilmaier, "High temperature oxidation behavior of an equimolar refractory metal-based alloy 20Nb-20Mo-20Cr-20Ti-20Al with and without Si addition," *Journal of Alloys and Compounds*, vol. 688, pp. 468-477, 2016.
- [50] M. M. L. Hitter and S. K. Varma, "Microstructural characterization, oxidation behavior, and properties of a new Al-Cu-Ni-Mn-Si non-BCC high entropy alloy at 600, 700, and 800C," *Journal of Materials Research and Technology*, vol. 23, pp. 680-686, 2023.
- [51] H. Yang, X. Liu, A. Li, R. Li, S. Xu, M. Zhang, P. Yu, S. Yu, M. Jiang, C. Huo and G. Li, "Effect of silicon addition on the corrosion resistance of Al<sub>0.2</sub>CoCrFe<sub>1.5</sub>Ni high-entropy alloy in saline solution," *Journal of Alloys and Compounds*, vol. 964, p. 171226, 2023.
- [52] C. Chen, S. Yuan, X. Li, J. Chen, W. Wang, R. Wei, T. Wang, T. Zhang, S. Wu, S. Guan and F. Li, "Microstructure, mechanical properties and corrosion resistance of an as-cast fine-structured Cr-Fe-Ni-Al-Si high entropy alloy," *Materials Today Communications*, vol. 35, p. 105523, 2023.
- [53] Y. Shi, L. Collins, C. Zhang, N. Balke, P. K. Liaw and B. Yang, "Homogenization of Al<sub>x</sub>CoCrFeNi high-entropy alloys with improved corrosion resistance," *Corrosion Science*, vol. 133, pp. 120-131, 2018.
- [54] Z. Niu, Y. Wang, C. Geng, J. Xu and Y. Wang, "Microstructure evolution, mechanical and corrosion behaviors of as-annealed CoCrFeNiMox (x = 0, 0.2, 0.5, 0.8, 1)," *Journal of Alloys and Compounds*, vol. 820, 2020.

## **Vita**

Celine Chiong attended the University of Texas at El Paso (UTEP) where she received her Bachelor of Science in Metallurgical and Materials Engineering in Spring of 2022. In her undergrad years, she worked as a teacher's assistant and as a volunteer scientific researcher in the Metallurgical, Materials, Biomedical Engineering Department. As a student, she was a member of the Tau Beta Pi Engineering Honor Society and Alpha Sigma Mu Honor Society.

During the summer of 2022, she completed an internship with the Air Force Research Laboratory in Albuquerque, NM providing her an opportunity to learn more about ultrashort pulse laser-materials interaction. Then in Fall of 2022, she enrolled for the master's degree in Metallurgical and Materials Engineering.

Currently, Celine is working as a graduate research assistant at UTEP. Collaborating with Stress Engineering Services for guidance and training for the development of the Electrochemistry Lab in the department. Diligently working on her research and learning new strategies along the way. After graduating, Celine will be participating in an internship at Aberdeen, Maryland for the Army Research Laboratory. She is enthusiastic in sharing her capabilities and learning new approaches from other experienced scientists and engineers that are already working in the field.

Contact Information: [ckcpinales15@gmail.com](mailto:ckcpinales15@gmail.com)